Available online at www.sciencedirect.com
ScienceDirect
Trans. Nonferrous Met. Soc. China 31(2021) 1529−1549
Transactions of Nonferrous Metals Society of China
www.tnmsc.cn

# Microstructure features and mechanical/electrochemical behavior of directionally solidified Al−6wt.%Cu−5wt.%Ni alloy

Adilson Vitor RODRIGUES[1,2], Thiago Soares LIMA[1], Talita Almeida VIDA[1], Crystopher BRITO[3], Amauri GARCIA[1], Noé CHEUNG[1]

1. Department of Manufacturing and Materials Engineering, University of Campinas - UNICAMP, Campinas, SP, 13083-860, Brazil;
2. Federal Institute of Education, Science and Technology of São Paulo - IFSP, Bragança Paulista, SP, 12903-600, Brazil;
3. São Paulo State University - UNESP, Campus of São João da Boa Vista, São João da Boa Vista, SP, 13876-750, Brazil

Received 31 July 2020; accepted 25 January 2021

**Abstract:** The effects of the addition of 5.0 wt.% Ni to an Al−6wt.%Cu alloy on the solidification cooling rate ($\dot{T}$), growth rate ($V_L$), length scale of the representative phase of the microstructure, morphology/distribution of intermetallic compounds (IMCs) and on the resulting properties were investigated. Corrosion and tensile properties were determined on samples solidified under a wide range of $\dot{T}$ along the length of a directionally solidified Al−6wt.%Cu−5.0wt.%Ni alloy casting. Experimental growth laws were derived relating the evolution of primary ($\lambda_1$) and secondary ($\lambda_2$) dendritic spacings with $\dot{T}$ and $V_L$. The elongation to fracture ($\delta$) and the ultimate tensile strength ($\sigma_U$) were correlated with the inverse of the square root of $\lambda_1$ along the length of the casting by Hall−Petch type experimental equations. The reinforcing effect provided by the addition of Ni in the alloy composition is shown to surpass that provided by the refinement of the dendritic microstructure. The highest corrosion resistance is associated with a microstructure formed by thin IMCs evenly distributed in the interdendritic regions, typical of samples that are solidified under higher $\dot{T}$.
**Key words:** Al−Cu−Ni alloys; as-cast microstructures; dendritic spacings; tensile properties; corrosion resistance

## 1 Introduction

Aluminum alloys have well-established industrial importance due to their excellent combination of mechanical, physical and tribological properties over other alloys. Some of the characteristics commonly presented by Al-based alloys are high specific strength, even at high temperatures, excellent stiffness, high wear and corrosion resistances, good electrical/thermal conductivities and malleability/formability. These properties can be obtained or modified through cold working, heat treatment or addition of alloying elements [1].

When added to Al casting alloys, Cu affects their mechanical strength and hardness at both ambient and elevated service temperatures, improves their machinability, increases the matrix hardness, but generally reduces their corrosion resistance [1]. The Al−Cu binary system is the basis of important cast commercial alloys as AA2014, AA2024, AA2099 and AA2219 [2]. The AA2219 alloy, which presents good weldability, high specific strength and heat resistance, is commonly used for strategic applications as components in the aerospace field [3]. In different studies in the literature, the AA2219 alloy has been associated

**Corresponding author:** Noé CHEUNG, E-mail: cheung@fem.unicamp.br
DOI: 10.1016/S1003-6326(21)65596-6

with various Cu contents, i.e., 5.8−6.8 wt.% Cu [4], 6.3 wt.% Cu [5] and 6.48 wt.% Cu [3]. The effects of the addition of the third component to the Al−6wt.%Cu binary alloy on microstructure and as-solidified properties have been examined in previous studies. FERREIRA et al [6] analyzed the microstructural development of an Al−6wt.%Cu alloy with the addition of 1 wt.% Si. OSÓRIO et al [7] examined the relationship between microstructure and electrochemical behavior of this alloy.

Al−Ni alloys stand out as promising candidates for high-temperature materials in harsh environmental applications [8]. Ni is almost insoluble in aluminum with solubility of about 0.05 wt.% at 640 °C and less than 0.005 wt.% at 450 °C [9]. Therefore, the formation of Ni-rich intermetallic compounds (IMCs) occurs even for low Ni concentrations [10]. Alloys containing Al−Ni based IMCs are mainly used for high temperature structural products, friction resistant coating materials and corrosion resistant coatings to protect from aggressive liquids and gases, as aircraft engines, turbine vanes, guide vanes of industrial steam turbines, etc [11]. The addition of Ni (up to 2%) increases the mechanical strength of high-purity aluminum but reduces the ductility due to the formation of many complex IMCs, such as $Al_3Ni$ [12].

The addition of Ni can improve the microstructure, mechanical properties, thermal stability, and hot tearing resistance of Al−Cu alloys [12]. When combined, Cu and Ni, form aluminides like $Al_3CuNi$ and $Al_7Cu_4Ni$, which are IMCs of high thermal stability and cannot be dissolved during solution heat treatments [10,13]. At elevated temperatures, the thermally stable IMCs, Cu or Ni containing phases, can impose a drag effect on grain boundaries and help to increase the elevated-temperature strength [14].

The microstructure of an alloy is at least as important as the composition in determining its properties. Prior to most of the heat treatments and metalworking processes, casting can be considered as the first metallurgical step, due to the transformation of molten metal into a solid form. It is worth mentioning the importance of studying solidification thermal parameters, such as the thermal gradient ($G_L$), the cooling rate ($\dot{T}$) and the growth rate ($V_L$), due to their direct influence on the microstructure, which play an important role not only in the resulting mechanical properties, but also in the corrosion behavior of metallic alloys [15,16]. One of the used approaches, is based on the directional solidification technique under unsteady-state regime, because it allows a wide range of thermal parameters to be examined in a single experiment, thus permitting extensive microstructural arrangements to be obtained. The evolution of $\dot{T}$ along unsteady-state solidification can synthesize the simultaneous influence of $G_L$ and $V_L$ on the microstructure, since $\dot{T}=G_L \cdot V_L$, and is therefore commonly correlated with the microstructure in unsteady-state solidification studies [17,18]. The development of correlations between thermal parameters and microstructure features and their further correlations with resulting properties are of industrial interest since they are useful to determine the better processing conditions to achieve required properties for a specific application. The substantial contribution of other solidification methods based on steady-state conditions must be highlighted, e.g., the Bridgman−Stockbauer technique, in which the influence of $G_L$ and $V_L$ can be independently analyzed [19−21].

The purpose of this work is to evaluate the role of the addition of 5.0 wt.% Ni to an Al−6wt.%Cu alloy, on solidification thermal parameters, the representative length scale of the microstructure and morphology/distribution of intermetallic compounds of a directionally solidified (DS) Al−6wt.%Cu−5.0wt.%Ni alloy casting. To the best knowledge of the present authors, the influence of the addition of Ni in a similar content to that of Cu in Al−Cu−Ni alloys, has not been explored in the literature so far in terms of mechanical and corrosion properties. The commercial version of cast Al−Cu alloys includes the 204 and 206 alloys series, which present high tensile strength and ductility at ambient and elevated temperatures [22]. However, not only these, but also other properties as yield strength, toughness and workability can be improved by the microstructural refinement of Al−Cu alloys [23], which is aimed in the present work with the addition of Ni. Corrosion and tensile properties will be determined on samples solidified under a wide range of $\dot{T}$ along the length of the DS Al−6wt.%Cu−5.0wt.%Ni alloy casting. Subsequently, interrelations of solidification thermal parameters, microstructural features, tensile

properties and corrosion resistance will be established.

## 2 Experimental

The Al−6.0wt.%Cu−5.0wt.%Ni alloy was prepared from commercially pure metals, and their compositions are summarized in Table 1. In order to prepare the alloy, firstly, Al was melted at 800 °C inside a SiC crucible coated with alumina; secondly Cu chips were added to the liquid bath, well mixed through mechanical agitation using a stainless-steel bar coated with alumina, and kept in the furnace for 45 min to permit the complete dissolution of Cu in the melt. Similar procedure was adopted in the subsequent addition of Ni. This step was repeated three times to guarantee the homogenization of the molten alloy. In order to eliminate the trapped gases inside the liquid, argon was injected for about 2 min. The molten alloy was then poured in a stainless-steel split mold and set into a water-cooled upward directional solidification apparatus (Fig. 1). Such experimental setup minimizes thermal and solutal convection since solidification progresses vertically upwards and segregation just ahead the solidification front generates a liquid that has a higher density as compared to that of the alloy melt. Cooling curves were obtained through 8 thermocouples positioned at different positions ($P$) from the cooled bottom of the casting, denominated $P0$, i.e., $P$=0 mm, taken as a reference. The temperature data were recorded at a frequency of 5 Hz using a Lynx data logger system. These data were used for further determination of the solidification thermal parameters, $\dot{T}$ and $V_L$.

Microstructural analyses were carried out in transversal and longitudinal samples extracted from different positions along the length of the directionally solidified (DS) casting. The microstructures were revealed using a 0.5% HF solution applied for 7 s while the macrostructure was revealed by Poulton's reagent, for 15 s. Micrographs were obtained by an optical Olympus inverted metallurgical microscope (model 41GX), and the ImageJ software was used to measure the primary ($\lambda_1$) and secondary ($\lambda_2$) dendrite arm spacings, with $\lambda_1$ being measured by the triangle method and $\lambda_2$ by the intercept method [24]. The solute profile along the length of the DS casting was obtained by an X-ray fluorescence spectrometer (XRF) (Rigaku-RIX3100). Selected samples of different positions from the cooled bottom of the casting ($P$=5 mm, $P$=20 mm and $P$=50 mm), which solidified at high, medium, and low cooling rates (14.71, 1.3 and 0.26 K/s) had their phases determined by X-ray diffraction (XRD)

**Table 1** Chemical compositions of metals used to prepare Al−Cu−Ni alloy (wt.%)

| Element | Al | Cu | Mg | Zn | Si | Sn | Ni | Mn | Fe | Pb | C | S | Co |
|---|---|---|---|---|---|---|---|---|---|---|---|---|---|
| Al | Bal. | 0.01 | 0.01 | 0.01 | 0.03 | – | – | – | 0.03 | – | – | – | – |
| Cu | – | Bal. | – | – | – | 0.009 | 0.008 | 0.008 | – | – | – | – | – |
| Ni | – | – | – | – | – | | Bal. | – | 0.004 | 0.002 | 0.004 | 0.002 | 0.017 |

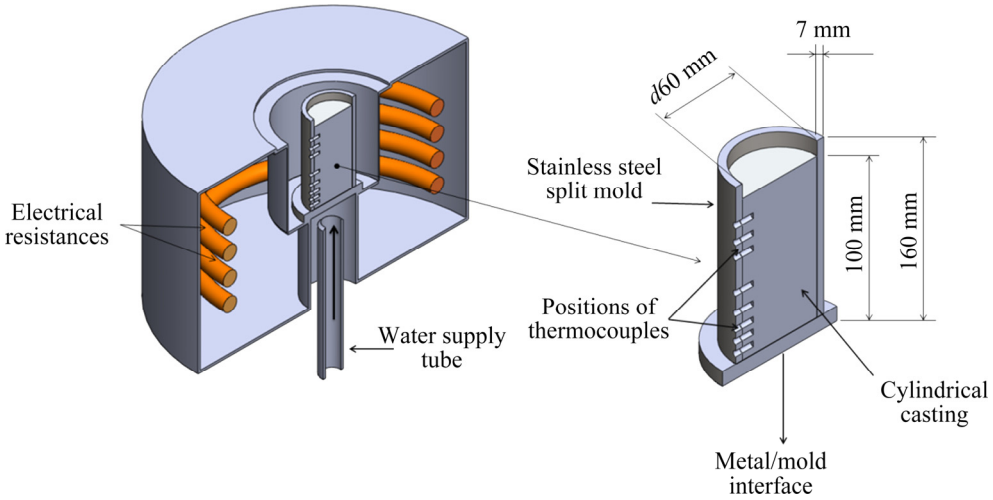


**Fig. 1** Schematic representation of water-cooled upward directional solidification apparatus and split mold

analysis (PAN analytical X'Pert PRO Materials Research Diffractometer XL) employing Cu $K_\alpha$ radiation with a wavelength of 0.15406 nm in the $2\theta$ range from 17° to 80°. A scanning electron microscope (SEM) (ZEISS-EVO-MA15) with an energy dispersive X-ray spectrometer (EDS) (QUANTA 650 FEG) was used to quantify Al, Cu and Ni distributions in the microstructure. Tensile tests were conducted according to the ASTM E 8M−04 Standard on a MTS 810 machine. Schematic representations of the extraction of the samples from the DS casting and of the measuring techniques used to quantify the length scales of the dendritic microstructures are presented in Fig. 2.

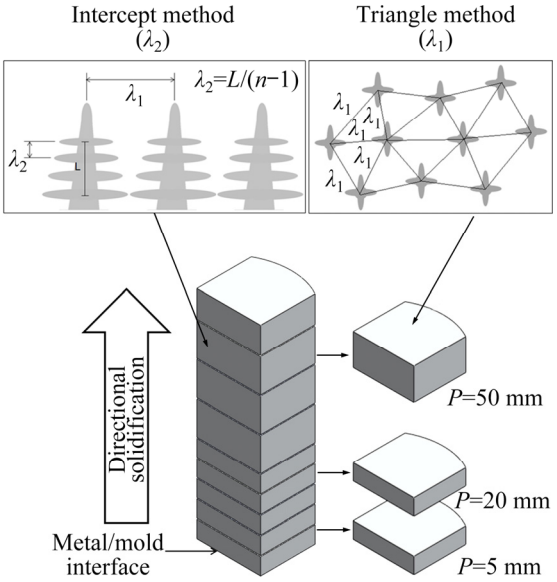


**Fig. 2** Schematic representation of extraction of samples and of measuring methods used to quantify length scale of dendritic microstructure (triangle method for $\lambda_1$ and intercept method for $\lambda_2$)

Potentiodynamic linear polarization tests were carried out at the same samples used for XRD analysis ($P$=5, 20 and 50 mm) using a 0.06 mol/L NaCl solution at 25 °C. A three-electrode cell setup was composed of (1) silver/silver chloride (Ag/AgCl) reference electrode, (2) platinum wire counter electrode, and (3) alloy samples as working electrodes, connected to a potentiostat/galvanostat Autolab (model PGSTAT 128N) (Fig. 3). The tests were performed in triplicate using samples with surface area of about 0.5 $cm^2$, ground up to 1 μm diamond paste finish and subjected to ultrasonic cleaning with distilled water and air drying to eliminate any dirt on the area to be tested. A galvanostatic tape, with a 0.5 $cm^2$ hole, which will permit contact between electrolyte and sample, is pre-placed on the working electrode. Posteriorly, the vessel is rigidly fixed with epoxy-based glue on the tape as well as sealed on the entire perimeter in contact with the galvanostatic tape. The samples were subjected to measurements at open circuit potential (OCP) for 1800 s, and then linear polarization tests were conducted at a scan rate of 0.167 mV/s from −0.200 to +0.350 V versus OCP. The corrosion potential ($\varphi_{corr}$) and the corrosion current density ($J_{corr}$) were determined by the Tafel's extrapolation method.

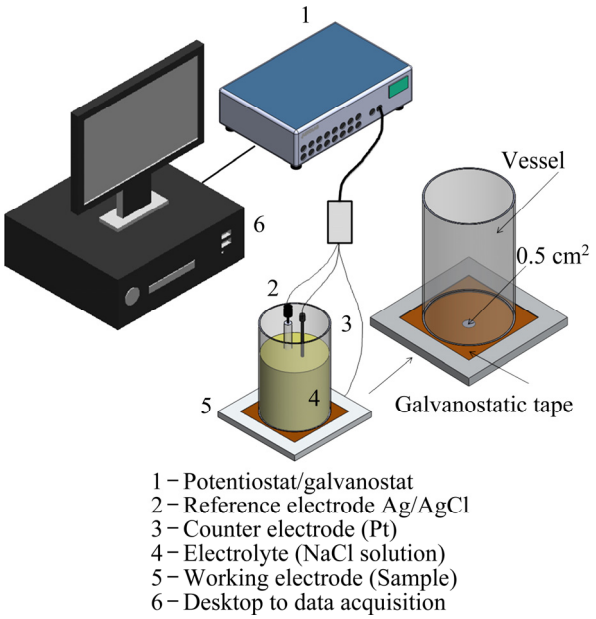


**Fig. 3** Experimental setup for polarization corrosion tests

## 3 Results and discussion

### 3.1 Al−Cu−Ni phase diagram

Figure 4 shows the partial Al−5wt.%Ni−Cu pseudo-binary phase diagram, obtained by the Thermo-Calc software, using the TTAL5 database. A dashed line indicates the composition of the alloy investigated in this work: Al−6.0wt.%Cu−5.0wt.%Ni. The solidification path (SP) predicted by Thermo-Calc, using the Scheil−Gulliver simulation, shows the mass fraction of solid phases as a function of temperature (Fig. 5). It is shown that the expected phases are: $\alpha$(Al) (FCC_A1), $Al_3Ni$, $Al_3Ni_2$, $Al_7Cu_4Ni$ ($\gamma$) and $Al_2Cu$ ($\theta$). The alloy composition favors the formation of Ni-rich IMCs, particularly $Al_3Ni$ that occurs under a rate that is slower than that of $Al_3Ni_2$ [25]. Phases with

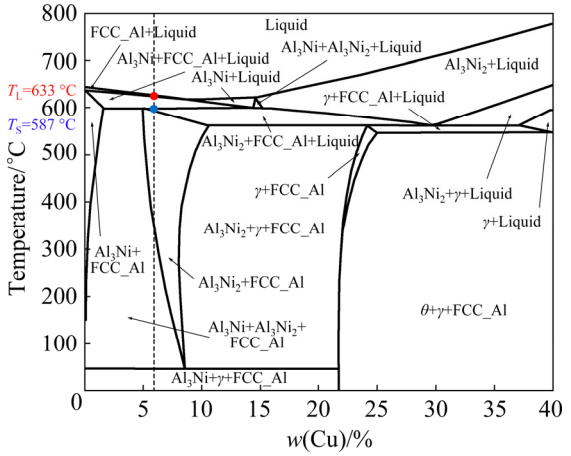


**Fig. 4** Partial Al−5wt.%Ni−Cu pseudo-binary phase diagram with dashed line indicating analyzed alloy composition (Thermo-Calc, TTAL5 database)

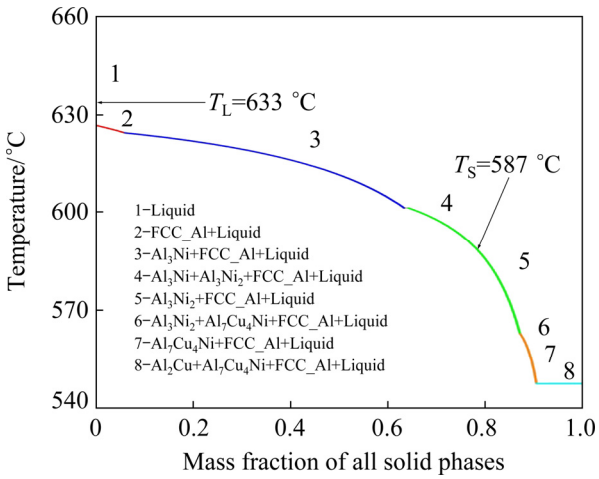


**Fig. 5** Al−6.0wt.%Cu−5.0wt.%Ni alloy solidification path calculated by Thermo-Calc software based on Scheil−Gulliver model (non-equilibrium conditions), TTAL5 database

low transformation rate can be suppressed in processes involving rapid solidification [26]. Therefore, in the further section of the present work, it will be verified if the high cooling rates of the vertical upward directional solidification process are able to inhibit the development of $Al_3Ni$, thus enabling the formation of $Al_3Ni_2$, which is reported to have a higher diffusion coefficient [27]. GARCÍA-ESCORIAL and LIEBLICH [28] observed the relation between the solidification rate and fractions of $Al_3Ni$ and $Al_3Ni_2$ particles produced by a gas atomization process. The results evidenced that the increase in cooling rates has generated higher quantities of $Al_3Ni_2$ and minor fractions of $Al_3Ni$.

### 3.2 Cooling rate, growth rate, thermal gradient and macrosegregation

The cooling curves obtained by the temperature readings of eight thermocouples positioned along the length of the DS casting are presented in Fig. 6. The analyses of these thermal profiles allowed the determination of the solidification thermal parameters: growth rate ($V_L$), cooling rate ($\dot{T}$) and thermal gradient ($G_L$). The time corresponding to the passage of the liquidus isotherm ($t_L$) by each thermocouple was obtained by the intersection of a dashed line drawn from the liquidus temperature ($T_L$) with each cooling curve. Figure 7(a) shows the position of each thermocouple from the metal/mold interface as a function of $t_L$. $V_L$ plotted in Fig. 7(b) resulted from the time-derivative of the function $P=f(t_L)$, where $P$ is the position of each thermocouple from the cooled bottom of the DS casting and $t_L$ is the time of passage of the liquidus isotherm by each thermocouple position. Figure 7(c) presents the $\dot{T}$ values obtained from the time-derivative of the function $T=f(t_L)$. Assuming that there is no considerable convection in the liquid, due to the experimental apparatus concept, it is possible to obtain $G_L$ from the ratio $G_L=\dot{T}/V_L$, as shown in Fig. 7(d). When compared to the results of a directionally solidified Al−5.0wt.%Cu−1.0wt.%Ni alloy [29], previously studied by the authors, the increase in the Ni content from 1.0 to 5.0 wt.% has decreased the aforementioned solidification thermal parameters. This behavior was also reported by CANTÉ et al [30] with the increase in the Ni content of upward directionally solidified binary Al−Ni alloys.

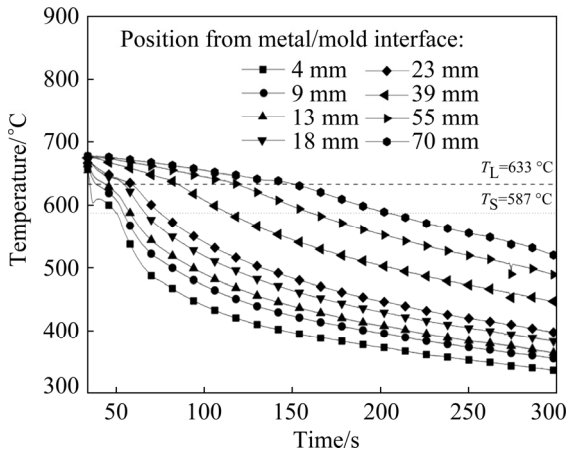


**Fig. 6** Experimental cooling curves along length of DS Al−6.0wt.%Cu−5.0wt.%Ni alloy casting

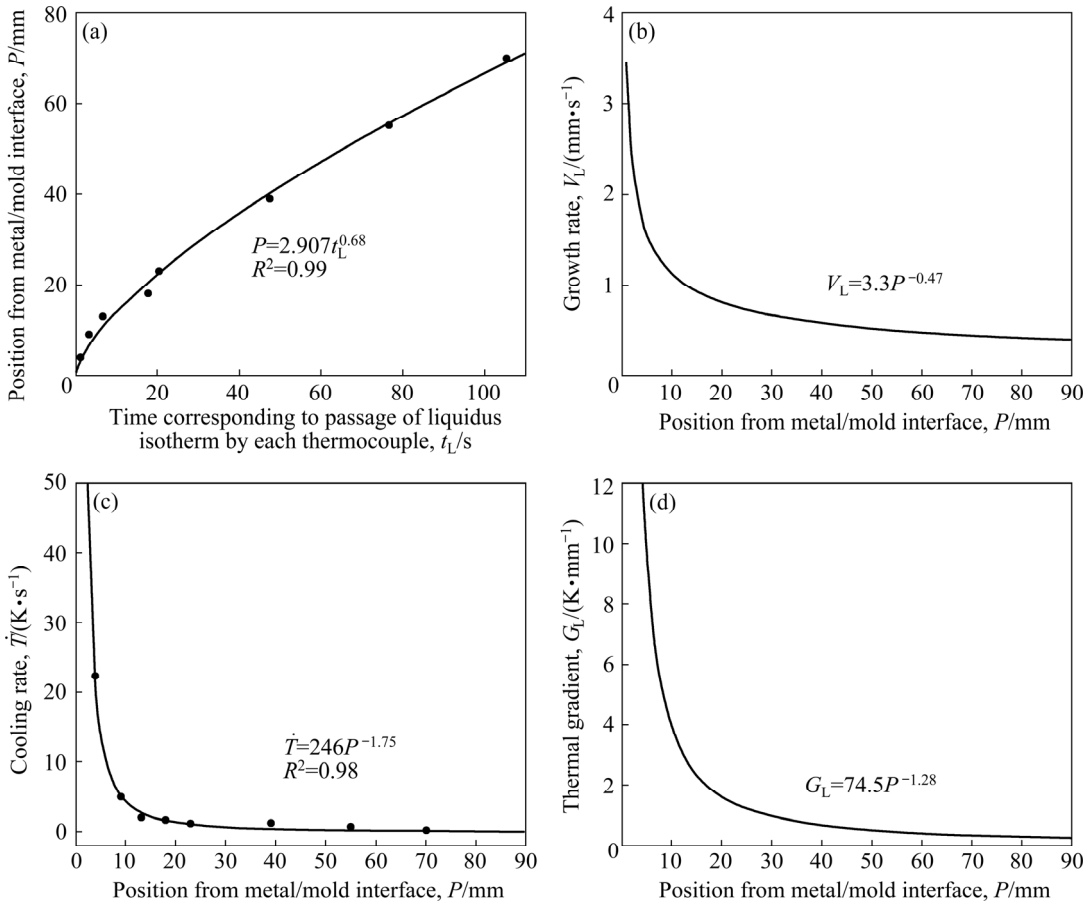


**Fig. 7** Thermal parameters along length of Al−6.0wt.%Cu−5.0wt.%Ni alloy casting: (a) Position of liquidus isotherm as function of time; (b) Growth rate ($V_L$); (c) Cooling rate ($\dot{T}$); (d) Thermal gradient ($G_L$)

Figure 8(a) shows the experimental Cu and Ni composition profiles along the length of the DS Al−6.0wt.%Cu−5.0wt.%Ni alloy casting determined by X-ray fluorescence (XRF). It is shown that both Cu and Ni contents remain almost constant and close to the alloy nominal composition for all the analyzed positions. Previous studies have reported the occurrence of inverse segregation of copper in directionally solidified Al−Cu and Al−Cu−Si alloys [31−34]. This phenomenon is a result mainly of the joint action of positive pressure in the liquid metal and volumetric contraction during solidification, which stimulates the flow of the interdendritic liquid in the opposite direction of the solid/liquid interface growth. In a previous work developed by the present authors [29], the role of alloy Ni content in blocking Cu inverse macrosegregation of DS Al−5.0wt.%Cu−1.0wt.%Ni and Al−15.0wt.%Cu−1.0wt.%Ni alloy castings was examined. The casting having 5.0 wt.% Cu presented only a slight inverse Cu segregation

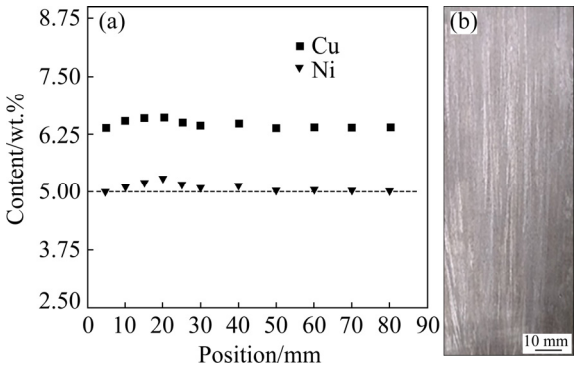


**Fig. 8** Copper and nickel profiles along length of DS casting obtained by XRF (a) and solidification macrostructure (b) of DS Al−6.0wt.%Cu−5.0wt.%Ni alloy casting

profile close to the cooled surface of the casting whereas for the casting having 15.0 wt.% Cu, Ni had practically no effect on the suppression of Cu inverse macrosegregation. In the case of the Al−6.0wt.%Cu−5.0wt.%Ni alloy, the higher amount of Ni promoted the formation of a higher fraction

of Ni-rich IMCs which, according to the alloy's solidification path shown in Fig. 5, nucleate first, acting as a barrier to the inverse flow of the eutectic liquid (Cu-rich) through the interdendritic channels during the final stages of solidification. Al−Cu−Ni alloys were used as example by MEHRABIAN and FLEMINGS [35] in their discussion about possible equations able to describe macrosegregation in ternary alloys. They emphasized that some alloying elements, such as Ni (with low solubility in Al), tend to form a second phase and segregate positively, while the solid solution components, such as Cu, segregate negatively. MOUTINHO et al [36] reported similar behavior in Al−Cu−Si alloys (Al−6.0wt.%Cu−1.0wt.%Si and Al−6.0wt.%Cu−4.0wt.%Si) where the increase in Si content from 1.0 to 4.0 wt.% induced a blockage to the inverse segregation of Cu, thus keeping the composition constant in 6.0 wt.% Cu all along the length of the casting. Further studies could be performed in order to determine the lowest Ni concentration in the range of 1−5 wt.%, which would be able to suppress the inverse segregation of Cu.

### 3.3 Macrostructure and microstructure

Figure 8(b) shows the macrostructure of the DS Al−6.0wt.%Cu−5.0wt.%Ni alloy casting. Columnar grains are aligned along the heat flow direction, with no evidence of columnar-to-equiaxed transition.

Figure 9 shows the transverse and longitudinal typical microstructures along the length of the Al−6.0wt.%Cu−5.0wt.%Ni alloy casting, essentially characterized by an Al-rich matrix of dendritic morphology. Samples from regions close to the water-cooled bottom were subjected to high solidification cooling rates, which generated refined microstructural arrangements. MURTY et al [37] reported that the microstructural refinement can be achieved during solidification by increasing cooling rates, through addition of solute elements or by inoculation.

Scanning electron microscopy (SEM) micrographs are shown in Fig. 10. The intermetallic compounds (IMCs) are localized in the interdendritic regions and are more refined when higher cooling rates are imposed. The high cooling rates involved in the water-cooled directional solidification process decrease the diffusion of solute atoms and drive the alloy to a non-equilibrium state, increasing the limit of solubility of solute elements in the aluminum matrix, thus affecting the formation of IMCs [38]. In the present work, solidification occurs at cooling rates far from equilibrium conditions inherent of phase diagram predictions. The literature reports, not only for Al−Cu alloys [39] but also for other Al-based alloys such as Al−Mn, Al−Cr and Al−Zr [40], that the increase in cooling rate during solidification leads to the increase in the solute solubility and thus to the generation of supersaturated solid solutions. Figures 11(a, b) show elemental SEM−EDS analysis (punctual) results of transverse sections of the Al-rich matrix at the positions *P*5 and *P*50, respectively. Each position presents an average Cu content of approximately 3.0 wt.%. Although constitutional supercooling may have occurred, it seems not to have been sufficient to limit the solubility of Cu in the Al-rich phase. Concerning the binary Al−Cu phase diagram, the maximum solubility of Cu in the Al-rich phase is 5.65 wt.% at the eutectic temperature (548 °C) [41], but the solubility decreases with the decrease in temperature reaching about 0.1 wt.% Cu at room temperature [42]. In the present work, the addition of Ni to the Al−6wt.%Cu alloy, has reduced the maximum solubility of Cu in Al to less than 2.5 wt.%, as can be seen in the equilibrium diagram of Fig. 4. It seems that the non-equilibrium conditions of the present directional solidification experiment have hindered the Cu diffusion, thus permitting supersaturated solid solution of Cu in Al matrix to be achieved.

The analyses of IMCs by elemental SEM−EDS (punctual and mapping) at the *P*5 and *P*50 positions are presented in Figs. 12 and 13, respectively. The results suggest the formation of $Al_7Cu_4Ni$ and other Ni-rich based IMCs. CHEN and THOMSON [43] used EBSD (electron backscatter diffraction) and SEM−EDS techniques to characterize the IMCs of an Al−12.0wt.%Si alloy with additions of 3.9 wt.% Cu, 2.8 wt.% Ni and 0.7 wt.% Mg. The authors co-sized the similarities between $Al_3Ni_2$ and $Al_7Cu_4Ni$ IMCs such as crystalline structures and lattice parameters, as well as the difficulties found in their differentiation. Therefore, the range of chemical compositions in terms of Cu and Ni becomes one of the main factors

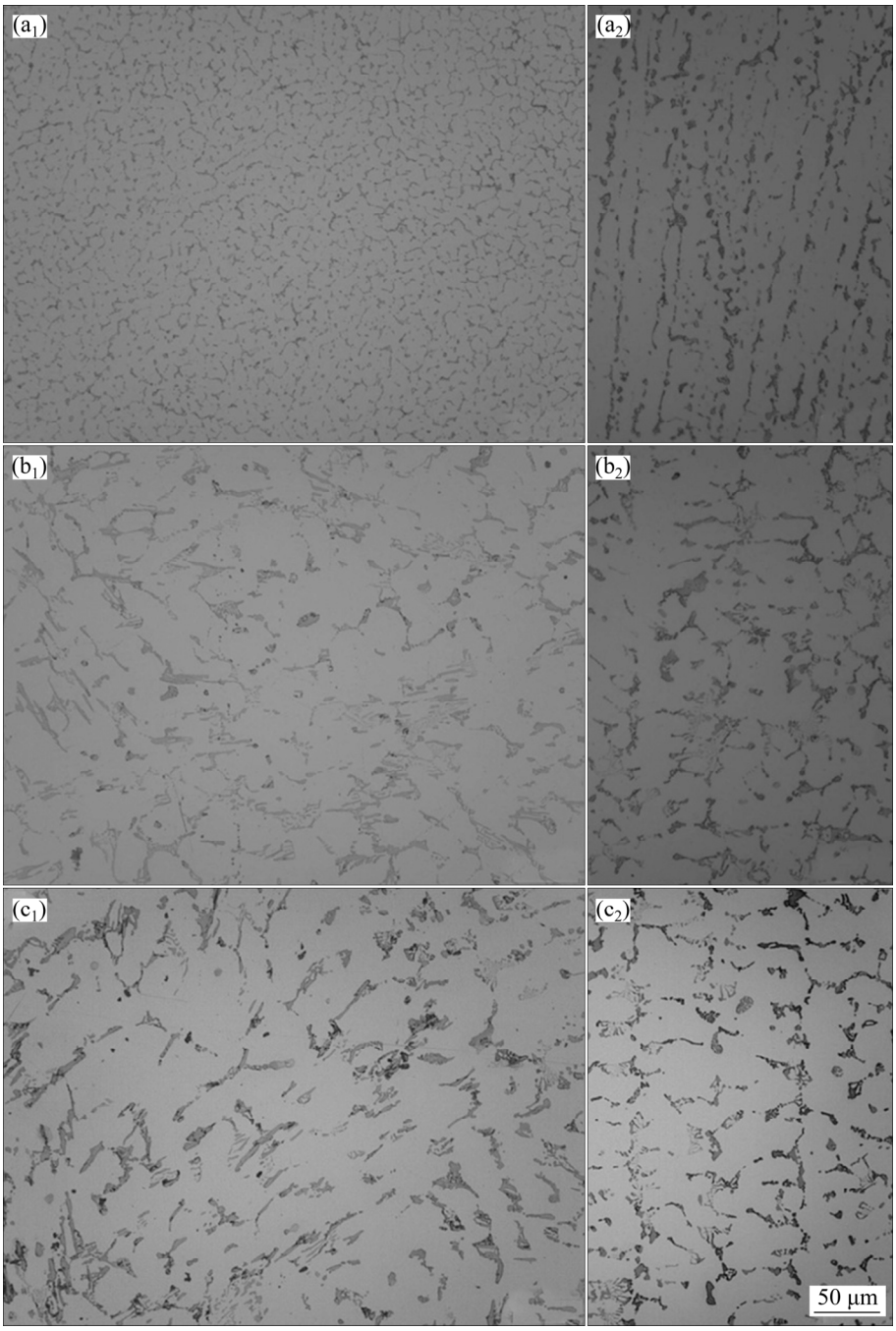


**Fig. 9** Transverse ($a_1$, $b_1$, $c_1$) and longitudinal ($a_2$, $b_2$, $c_2$) micrographs obtained by optical microscopy for different positions (*P*) along length of Al−6.0wt.%Cu−5.0wt.%Ni alloy casting: ($a_1$, $a_2$) *P*=5 mm; ($b_1$, $b_2$) *P*=20 mm; ($c_1$, $c_2$) *P*= 50 mm

for the identification of these two IMCs. They described the Ni relation (Ni)/(Ni+Cu) for each one of the IMCs as higher than 40% for $Al_3Ni_2$, between 6% and 39% for $Al_7Cu_4Ni$ and below 5% for $Al_2Cu$. Concerning the IMCs morphologies identified, CHEN and THOMSON [43] reported a thick plate-like morphology for $Al_3Ni_2$ and WARMUZEK [44] found irregular plates (branched) for $Al_7Cu_4Ni$ in the microstructure of multicomponent Al−Si based alloys (AlSi13Mg1CuNi and AlSi21CuNi). In the Al−5.0wt.%Cu−1.0wt.%Ni alloy, previously studied by the present authors [29], the higher amount of Cu, as compared to Ni, decreased the stability of the $Al_3Ni_2$ IMC. However, in this work, the increase in the Ni alloying content, associated with high solidification cooling rates, was able to

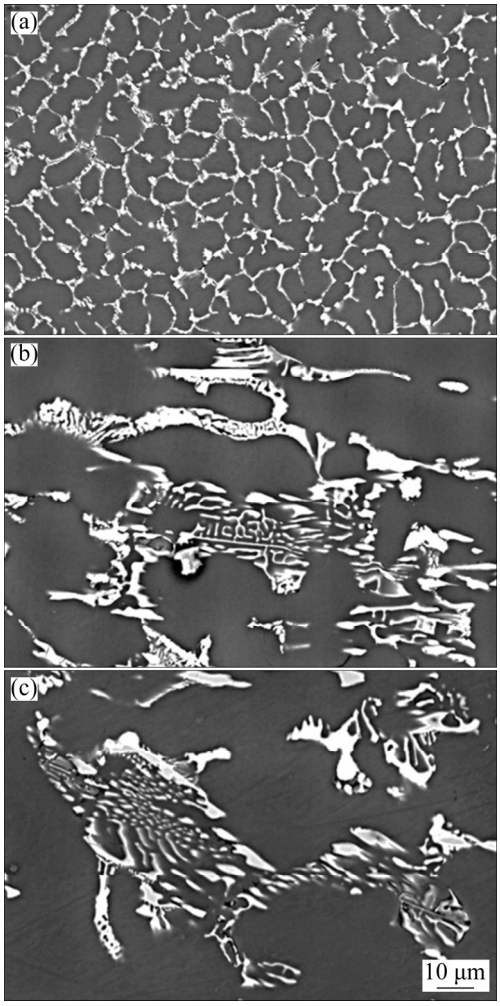


**Fig. 10** Scanning electron microscopy images for *P*=5 mm (a), *P*=20 mm (b) and *P*=50 mm (c) positions from cooled bottom of Al−6.0wt.%Cu−5.0wt.%Ni alloy casting

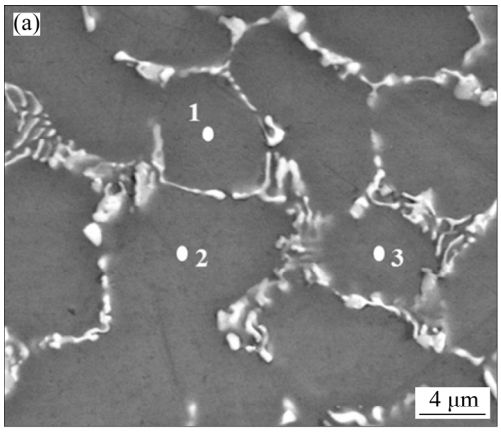


| Point | Content/wt.% | | |
|---|---|---|---|
| | Al | Cu | Ni |
| 1 | 96.20 | 3.32 | 0.48 |
| 2 | 96.50 | 3.03 | 0.47 |
| 3 | 96.41 | 2.87 | 0.72 |

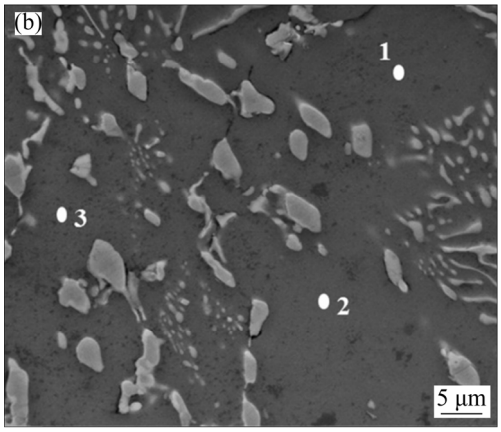


| Point | Content/wt.% | | |
|---|---|---|---|
| | Al | Cu | Ni |
| 1 | 96.26 | 3.07 | 0.67 |
| 2 | 96.66 | 2.70 | 0.64 |
| 3 | 95.84 | 3.41 | 0.75 |

**Fig. 11** Elemental SEM−EDS analysis results of Al matrix for *P*=5 mm (a) and *P*=50 mm (b) positions from cooled bottom of Al−6.0wt.%Cu−5.0wt.%Ni alloy casting

provide the formation of $Al_3Ni_2$. Calculation of Ni relations for the Al−6.0wt.%Cu−5.0wt.%Ni alloy associated with morphology and elemental SEM−EDS mappings suggests the formation of a higher fraction of $Al_3Ni_2$ with thick plate-like morphology. Additionally, in Fig. 13, it is possible to distinguish three phases with different contrasts. CHEN and THOMSON [43] examined a specific particle that presented three different contrast regions in an EBSD image. Based on the difference in their Ni contents, observed through EDX maps, it was assumed by these authors that the particle should be formed by $Al_3Ni_2$, $Al_7Cu_4Ni$ and $Al_2Cu$. KUNDIN et al [45] have also observed, through SEM images, different contrasts between $Al_3Ni$ and $Al_3Ni_2$ IMCs in a study about phase transitions and structure formation in an Al−4.5at.%Cu−11at.%Ni alloy. Similar results can be observed at *P*=50 mm (Fig. 13) of the Al−6.0wt.%Cu−5.0wt.%Ni alloy casting, which suggests the formation of $Al_3Ni_2$ (darker phase with higher Ni content), $Al_7Cu_4Ni$ (phase with intermediate contrast and Ni content) with irregular plates morphology and $Al_2Cu$ (lighter phase with lower Ni content) in non-lamellar format. This difference of contrasts can be explained by the higher atomic number of Cu (29) as compared to that of Ni (28). The BSE (backscattered electrons) technique consists of incident electrons reflected back from a target specimen, which are detected to construct a scanning electron image of the specimen.

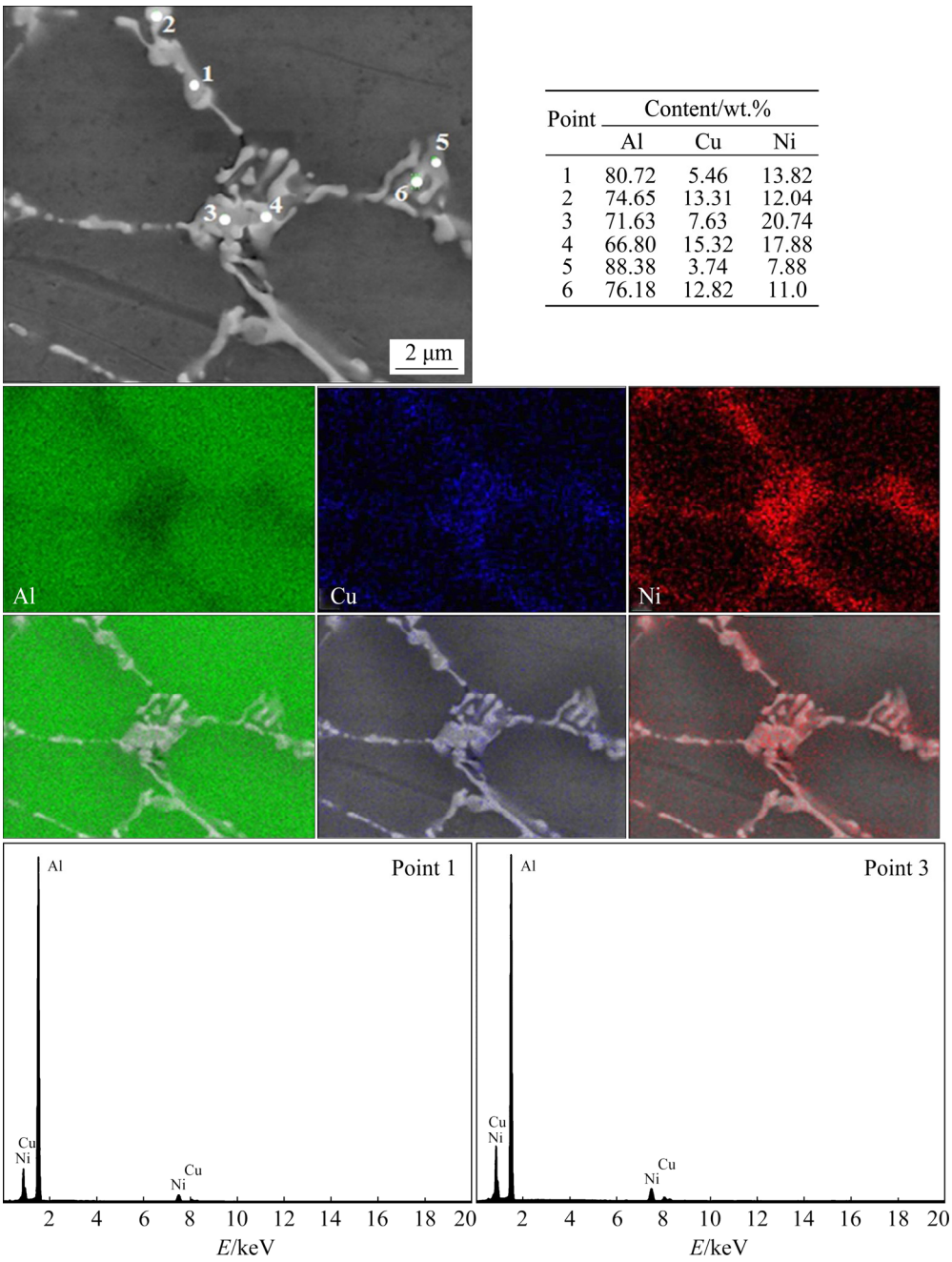


| Point | Content/wt.% | | |
|---|---|---|---|
| | Al | Cu | Ni |
| 1 | 80.72 | 5.46 | 13.82 |
| 2 | 74.65 | 13.31 | 12.04 |
| 3 | 71.63 | 7.63 | 20.74 |
| 4 | 66.80 | 15.32 | 17.88 |
| 5 | 88.38 | 3.74 | 7.88 |
| 6 | 76.18 | 12.82 | 11.0 |

**Fig. 12** Elemental SEM−EDS (punctual and mappings) and qualitative intensities for $P$=5 mm position from cooled bottom for Al−6.0wt.%Cu−5.0wt.%Ni alloy casting

The BSE emission coefficient ($\eta$) depends on the target atomic number ($Z$). Specimens consisting of only a single-phase have $Z$ and hence $\eta$ constants, resulting in images with uniform intensity and no contrast. However, in polyphase specimens, $Z$ and $\eta$ vary from phase to phase in such way that the BSE image contains different intensities and contrasts, and in such cases, phases with higher $Z$ values present brighter appearance [46]. The atomic numbers of Cu and Ni are 29 and 28, respectively. This can explain the difference of image contrasts among the phases observed, with Cu-rich phases appearing brighter than Ni-rich phases. To complement the analysis and reinforce the presented values of elemental analysis, the qualitative peak intensities of Al, Cu and Ni of some points are additionally presented in Figs. 12 and 13. As expected, all spectra reveal prominent peaks for Al. The analyses of Points 1 and 3 from Fig. 12 and Point 1 from Fig. 13 show

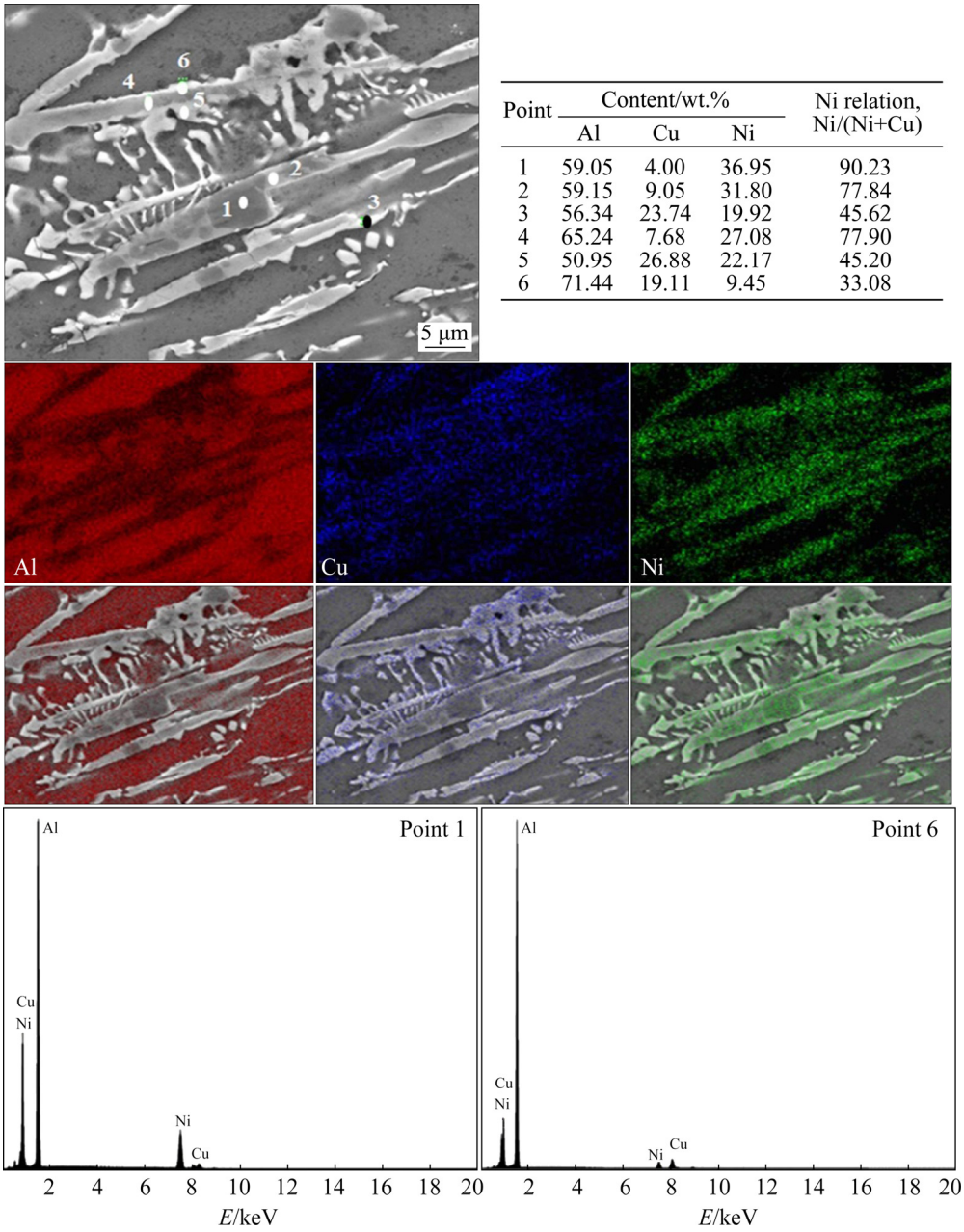


| Point | Content/wt.% | | | Ni relation, Ni/(Ni+Cu) |
|---|---|---|---|---|
| | Al | Cu | Ni | |
| 1 | 59.05 | 4.00 | 36.95 | 90.23 |
| 2 | 59.15 | 9.05 | 31.80 | 77.84 |
| 3 | 56.34 | 23.74 | 19.92 | 45.62 |
| 4 | 65.24 | 7.68 | 27.08 | 77.90 |
| 5 | 50.95 | 26.88 | 22.17 | 45.20 |
| 6 | 71.44 | 19.11 | 9.45 | 33.08 |

**Fig. 13** Elemental SEM−EDS (punctual and mappings) and qualitative intensities for *P*=50 mm position from cooled bottom of Al−6.0wt.%Cu−5.0wt.%Ni alloy casting

higher peaks related to Ni as compared to Cu peaks, which corroborates the numerical values presented. The analysis of Point 6 from Fig. 13 evidences a kind of inversion in the intensity of peaks between Cu and Ni, now with a predominance of Cu. Similar morphologies of IMCs were observed by MOTLAGH et al [47] in the study of the Al 1100 alloy coated with a powder mixture of "Ni+14Al+CuO+2NiO". The authors suggested a reaction between Al and Cu in the liquid state with $Al_3Ni_2$, forming $Al_7Cu_4Ni$ during cooling by the reaction of $L+Al_3Ni_2 \rightarrow (Al)+Al_7Cu_4Ni$. This agrees with the peritetic reaction previously observed in the solidification path of the Al−6.0wt.%Cu−5.0wt.%Ni alloy (Fig. 5). The considerable Cu amount detected in the IMCs, not only by punctual SEM−EDS analysis but also visually verified (Figs. 12 and 13), suggests the interruption of the peritetic reaction, permitting the coexistence of $Al_3Ni_2$ and $Al_7Cu_4Ni$.

The X-ray diffraction (XRD) patterns of samples from positions *P*=5 mm, *P*=20 mm and *P*=50 mm are presented in Fig. 14. The results clearly evidence the formation of $\alpha$(Al) and $Al_2Cu$.

On the other hand, crystallographic similarities between the $Al_3Ni_2$ and $Al_7Cu_4Ni$ IMCs make their diffraction peaks close to each other, being difficult to distinguish one from another. These peaks are identified as $Al_7Cu_4Ni/Al_3Ni_2$ in the diffractograms. MOTLAGH et al [47] reported the same difficulty in the determination of these IMCs by a XRD technique for the Al 1100 alloy.

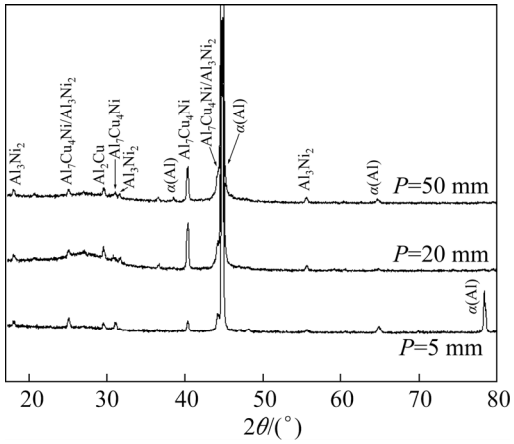


**Fig. 14** XRD patterns of samples from positions $P$=5 mm, $P$=20 mm and $P$=50 mm from cooled bottom of Al−6.0wt.%Cu−5.0wt.%Ni alloy casting

### 3.4 Solidification thermal parameters and microstructural spacings

Figure 15 shows the evolution of the primary dendrite arm spacing ($\lambda_1$), mean values and range of maximum and minimum experimental values, for Al−6.0wt.%Cu−5.0wt.%Ni alloy casting. Average values of $\lambda_1$ measured at different positions along the length of the DS casting are related to the cooling rate ($\dot{T}$) and the growth rate ($V_L$) by the experimental growth laws: $\lambda_1 = 71.7\dot{T}^{-0.55}$ and $\lambda_1 = 56V_L^{-1.1}$, respectively. These laws are compared to results of Al−5.0wt.%Cu−1.0wt.%Ni alloy [29], Al−5.0wt.%Cu alloy [48] and Al−1.0wt.%Ni/Al−4.7wt.%Ni [49] hypoeutectic binary alloys. Although ROCHA et al [48] reported that $\lambda_1$ was proven to be independent of the Cu content of Al−5wt.%Cu, Al−8wt.%Cu and Al−15wt.%Cu alloys, and CANTÉ et al [49] stated a similar conclusion with respect to the Ni content of Al−1wt.%Ni and Al−4.7wt.%Ni alloys, the addition of 1.0 wt.% Ni to Al−5.0wt.%Cu alloy promoted a decrease in $\lambda_1$ as compared to the corresponding values of the Al−5.0wt.%Cu binary alloy, for the same $\dot{T}$ and $V_L$ values. The increase in the Ni alloying content from 1.0 to 5.0 wt.% implied a decrease in $\lambda_1$ to values even lower than those reported for Al−Ni binary alloys. The effects of solute segregation ahead the solid/liquid interface on the destabilization of the solidification front of multicomponent alloys is still unknown. However, it is reported that the higher the solute content is in this region, the higher the constitutional undercooling will be, thus favoring the reduction in the length scale of the microstructure [50]. Therefore, the increase in Ni content from 1 to 5 wt.% for the Al−6wt.%Cu−Ni alloys has probably induced the decrease in $\lambda_1$.

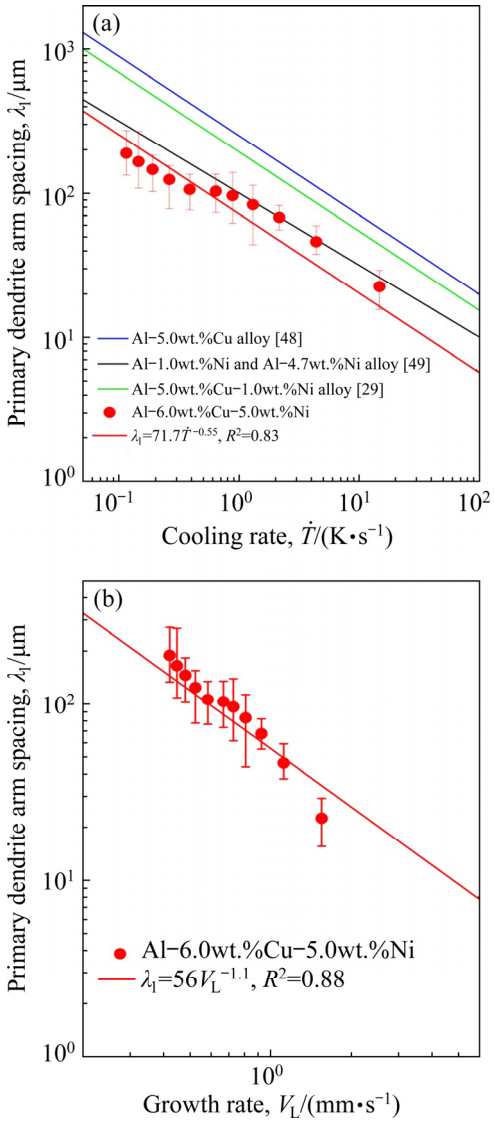


**Fig. 15** Primary dendrite arm spacing evolution as function of cooling rate ($\dot{T}$) (a) and growth rate ($V_L$) (b) for Al−6.0wt.%Cu−5.0wt.%Ni alloy casting

The evolution of the secondary dendrite arm spacing ($\lambda_2$) is presented as a function of $\dot{T}$ and $V_L$ in Figs. 16(a) and 16(b), respectively. Although the use of −1/3 and −2/3 exponents in the experimental

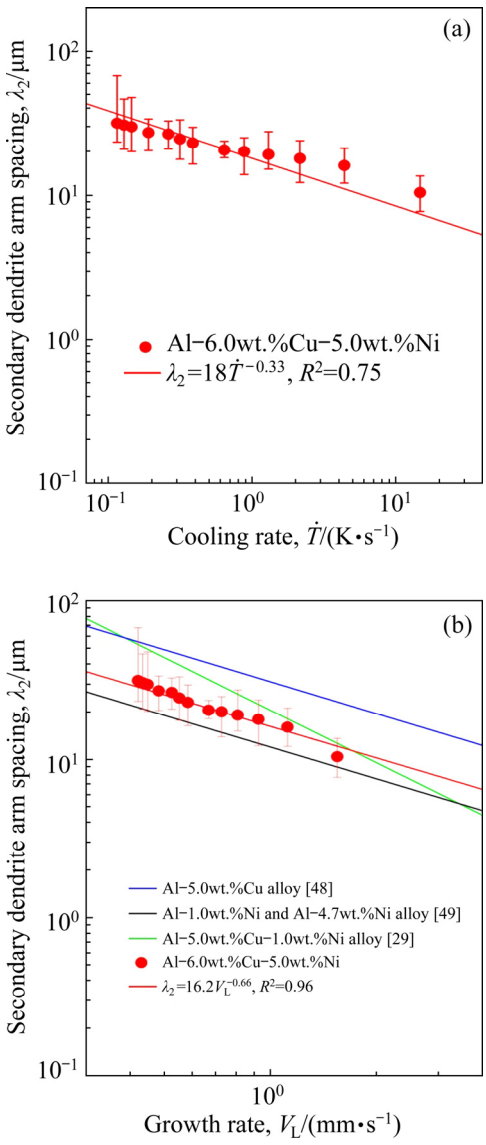


**Fig. 16** Secondary dendrite arm spacing evolution as function of cooling rate ($\dot{T}$) (a) and growth rate ($V_L$) (b) for Al−6.0wt.%Cu−5.0wt.%Ni alloy casting

laws relating $\lambda_2$ to $\dot{T}$ and to $V_L$, respectively, were reported to be effective to describe the growth of secondary dendritic branches of some ternary Al-based alloys [36,51,52], recently SILVA et al [53] proposed the use of exponents with different values for $\lambda_2$ and $\lambda_3$ for ternary Sn−Bi−(Cu,Ag) alloys. As reported in a previous study by the present authors for the Al−5.0wt.%Cu−1.0wt.%Ni alloy [29], the use of −0.55 and −1.1 exponents was shown to be appropriate to correlate $\lambda_1$ and $\lambda_2$ to $\dot{T}$ and $V_L$, respectively. However, the increase in the alloy Ni content required the use of −1/3 and −2/3 exponents for a satisfactory fit to the experimental scatter. This is in accordance with the exponents used for the Al−5.0wt.%Cu [48] and Al−Ni binary alloys [49] plotted in Fig. 16(b) for comparison purposes. The results show that the highest profile of $\lambda_2$ is observed for the Al−5.0wt.%Cu alloy, the lowest one to hypoeutectic Al−Ni alloys (Al−1.0wt.%Ni and Al−4.7wt.%Ni) and in between the profile of the ternary alloys. EASTON and STJOHN [54] in their review on grain refinement of Al alloys, discussed about the growth restriction factor (GRF), which is a measure of the growth-restricting effect of solute elements on the growth of the solid−liquid interface of new grains. The GRF is related to the composition of the alloy through the equation $mC_0(k-1)$, where $m$ is the slope of the liquidus line, $C_0$ is the alloy solute content and $k$ is the partition coefficient between the equilibrium concentrations of the solid and liquid at the growing interface [54]. The segregating powers, $m(k-1)$, of some elements in Al are given by the authors and for Cu and Ni these values are 2.8 and 3.3, respectively [54]. The solute affects the dendritic growth and creates a constitutionally undercooled zone ahead the solidification front. This undercooled zone facilitates nucleation of new grains [55]. The greater the undercooling parameter is, the stronger the grain refiner will be [56]. CHANDRASHEKAR et al [55] in their work about the effect of GRF on grain refinement of Al alloys, concluded that the growth rate is inversely proportional to GRF. The higher GRF is, the finer the grains will be [56]. In this sense, Ni seems to be a more effective refiner of the microstructure as compared to Cu. The increase in the Ni content from 1.0 to 5.0 wt.% in the ternary alloys followed the aforementioned tendency presented by binary alloys during directional solidification, which resulted in the decrease of $\lambda_2$.

### 3.5 Microstructural features vs tensile properties

The elongation to fracture ($\delta$) and the ultimate tensile strength ($\sigma_U$) are correlated with the inverse of the square root of $\lambda_1$ by Hall−Petch type experimental equations in Figs. 17(a) and 17(b), respectively. In order to observe the effects of the addition of Ni to the Al−6wt.%Cu alloy, a correlation obtained in a previous study for the Al−4.0wt.%Cu alloy [52] has been included for comparison purposes. In general, a lower $\lambda_1$ contributes to higher values of $\sigma_U$ because this enables a more homogeneous distribution of

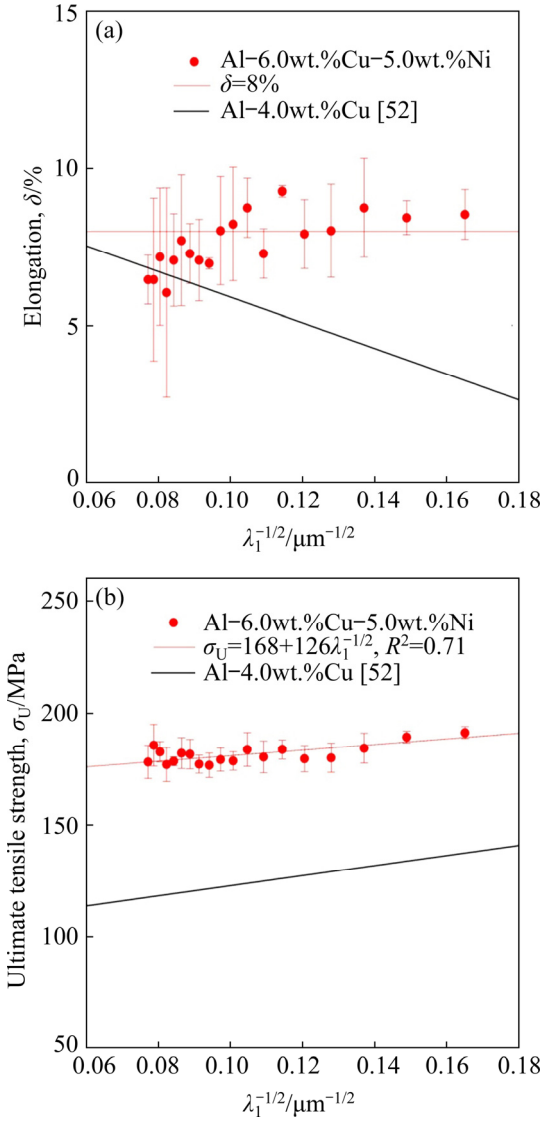


**Fig. 17** Elongation (a) and ultimate tensile strength (b) as function of $\lambda_1^{-1/2}$ for Al−6.0wt.%Cu−5.0wt.%Ni alloy casting

intermetallic compounds in the interdendritic regions. This behavior is observed for the Al−4.0wt.%Cu alloy since the refinement of the dendritic microstructure is accompanied by significant increase in $\sigma_U$ and consequently decrease in $\delta$. The addition of 5.0 wt.% Ni (Al−6.0wt.%Cu−5.0wt.%Ni alloy) resulted in the highest values of $\sigma_U$. KIM et al [57] studied the microstructure, mechanical properties and dynamic mechanical properties of reinforced in-situ Al−$Al_3Ni$ eutectic composites with different Cu contents (0, 5, 10, 15, 20 and 25 at.%). They observed that the increase in strength induced by the addition of Cu, results from the action of multiple strengthening mechanisms as: (1) solid-solution hardening due to higher solubility of Cu in Al, (2) formation of different IMCs with higher hardness and modulus and (3) Hall−Petch strengthening due to the ultrafine lamellar structure of the eutectic with decreased lamellar spacing. Similarly, in the present work, the higher values of $\sigma_U$ of the Al−6.0wt.%Cu−5.0wt.%Ni alloy, as compared to those of the Al−4.0wt.%Cu alloy, seem to be related to the simultaneous action of: (1) the supersaturated solid-solution of Cu in the Al matrix, (2) the formation of the Ni containing IMCs of $Al_3Ni_2$ and $Al_7Cu_4Ni$, and (3) the microstructural refinement ($\lambda_1$ and $\lambda_2$) promoted by the addition of 5.0 wt.% Ni. The ultimate tensile strength of the Al−6.0wt.%Cu−5.0wt.%Ni alloy can be expressed as a series of additive effects: $\sigma_U=\sigma_{Solid\text{-}solution}+\sigma_{IMCs}+\sigma_{microstructual\text{-}refinement}$. CHEN et al [58] concluded, through nanoindentation tests in multicomponent Al−Si casting alloys, that the hardness of IMCs increases as the Ni relation (Ni/(Ni+Cu)) of the AlCuNi phases increases ($Al_3Ni_2$>$Al_7Cu_4Ni$>$Al_2Cu$). Therefore, AlCuNi IMCs can present variations in the mechanical properties depending on such Ni relation. It is worth noting the positive effect on the tensile properties due to the enveloping process of the Cu-rich IMCs growing over the $Al_3Ni_2$ particles, as reported by KUNDIN et al [59], shown in Fig. 13. The $Al_3Ni_2$ phase is reported [59] to have a morphology characterized by crystals with sharp edges, which can induce deleterious effects especially on the elongation behavior. The Cu-rich IMCs envelope hinders this harmful characteristic to the alloy. BASAK et al [60] studied the influence of the addition of Ni (from 0% to 8wt.% with an interval of 2 wt.%) to several Al−Si alloys (6, 9 and 12 wt.% Si) with a constant Fe content of 2 wt.% for all alloys. Beyond the gravity cast applied for obtaining the alloy set, selected alloys containing 9 wt.% Si, 12 wt.% Si and 2 wt.% Fe, with varying Ni content up to 4 wt.%, were made using high pressure die casting (HPDC). The results showed that irrespective of the Si content and the casting technique, alloy compositions beyond 4 wt.% Ni had the ductility reduced. Despite the huge difference in the cooling rates that determines the interdendritic spacings, the authors safely assumed that ductility is not dependent on the size of dendrites, once this property does not vary much from gravity cast to HPDC process for a given composition. However, the refined microstructures obtained by high

pressure die casting promoted significant rises in both yield and ultimate tensile strengths as compared to alloys obtained by gravity cast. In the present work, similar behavior is observed. The tensile properties of the alloy without Ni (Al−4.0wt.%Cu) were more sensitive to variations in $\lambda_1$ while the alloy containing Ni (Al−6.0wt.%Cu−5.0wt.%Ni) has shown only slight increase in the ultimate tensile strength for more refined microstructures, that is, for lower values of $\lambda_1$, whereas an appreciable average elongation of 8% for the entire microstructural spectrum analyzed was observed. Therefore, in this work, the amount of Ni in the Al−6.0wt.%Cu−5.0wt.%Ni alloy seems to suppress the effect of cooling rate variations along the casting length (different $\lambda_1$ values) on the tensile properties.

### 3.6 Microstructural features vs corrosion properties

Figure 18 shows the comparison of the experimental linear polarization profiles of Al−6wt.%Cu−5wt.%Ni alloy samples extracted from Positions *P*5, *P*20 and *P*50 from the cooled bottom of the DS casting. These profiles are potted between potentials of −0.650 and −0.400 V (vs Ag/AgCl). The polarization profiles allowed the values of corrosion current densities ($J_{corr}$) and corrosion potentials ($\varphi_{corr}$) in a solution of 0.06 mol/L NaCl at room temperature, 25 °C, to be determined. The average values of $\varphi_{corr}$ and $J_{corr}$ for the examined samples were determined by extrapolation from Tafel's plots considering both the anodic and cathodic branches of the polarization curves.

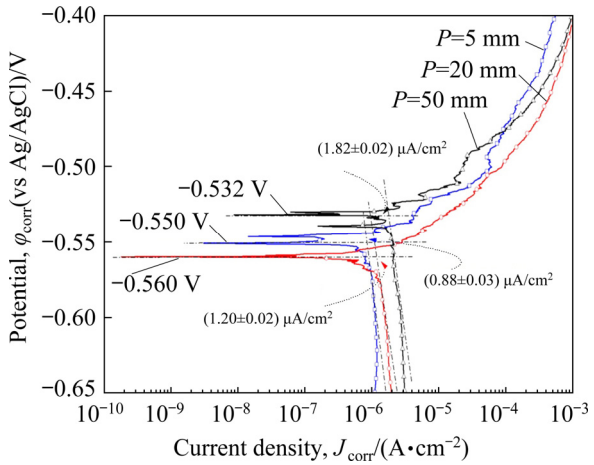


**Fig. 18** Experimental polarization curves of Al−6wt.%Cu−5wt.%Ni samples in 0.06 mol/L NaCl solution at 25 °C

The examined samples of the Al−6wt.%Cu−5wt.%Ni alloy casting have corrosion potentials ($\varphi_{corr}$) varying between −0.560 and −0.532 V (vs Ag/AgCl), presenting a small difference of 0.20 V when the corrosion potentials of all samples are compared. The lowest $J_{corr}$ is (0.88±0.03) μA/cm$^2$ for $\varphi_{corr}$=−0.550 V (vs Ag/AgCl), for the *P*5 sample. Although the *P*50 sample shows a nobler corrosion potential ($\varphi_{corr}$), its $J_{corr}$ is considerably higher as compared to that of the *P*20 and *P*5 samples (*P*50>*P*20>*P*5). This indicates that the *P*50 sample is more susceptible to corrosion, since the corrosion rate is an indicative of the material's behavior against corrosion. The values of corrosion potential ($\varphi_{corr}$), corrosion current density ($J_{corr}$), cooling rate, primary dendritic spacing ($\lambda_1$), secondary dendritic spacing ($\lambda_2$), and fraction of intermetallics ($F_{IMC}$) are given in Table 2. The *P*5 sample (with the highest cooling rate) has lower values of $\lambda_1$ and $\lambda_2$, (22.53±3.4) μm and (1.43±1.8) μm, respectively. Such morphological parameters of *P*5 are associated with $J_{corr}$ of 0.88 μA/cm$^2$ and greater resistance to corrosion (CR) of 1.14 cm$^2$/μA, (CR=1/$J_{corr}$), considered by some authors [29,61,62] as an indicator of the susceptibility to corrosion for a given aggressive medium. In contrast, the *P*50 sample (with lower cooling rate) has higher dendritic spacings, $\lambda_1$=(124.23±19.12) μm and $\lambda_2$=(26.55±3.5) μm and higher $J_{corr}$(=1.82 μA/cm$^2$) and CR(=0.54 cm$^2$/μA). These results show that the corrosion current density increases with increasing distance from the cooled base of the DS casting (coarser microstructure), indicating that the *P*5 position is less susceptible to corrosion. This also confirms the influence of the length scale of the microstructural morphology on the corrosion resistance tendency.

The corrosion rate ($R_C$) is another parameter that can be used to check the corrosion behavior of metallic alloys. This parameter allows the conversion of the corrosion rate obtained by electrochemical techniques into current density units (μA/cm$^2$) for penetration depth unit per time unit (μm/year). Its values can be obtained based on the ASTM G102−89 Standard, and calculated according to the following equations [63,64]:

$$R_C = K_1 \cdot \frac{J_{corr}}{\rho} \cdot W_E \quad (1)$$

$$W_E = 1 \Big/ \sum \frac{n_i f_i}{W_i} \quad (2)$$

where $R_C$ is the corrosion rate (μm/year), $K_1$= $3.27\times10^{-3}$ mm·g/(μA·cm·year), $J_{corr}$ is the corrosion current density (μA/cm$^2$), and $\rho$ is the density of the alloy (g/cm$^3$); $W_E$ is the alloy equivalent mass, $n_i$ is the valence of the $i$th element of the alloy, $f_i$ is the mass fraction of the $i$th element in the alloy and $W_i$ is the atomic mass of the $i$th element of the alloy.

The $R_C$ values corroborated the CR values, confirming that the P5 sample has a lower degradation rate when all samples are compared. The $R_C$ values are summarized in Table 2.

These considerations agree with recent studies that reported the corrosion resistance of ternary Al−5wt.%Cu−1wt.%Ni and Al−15wt.%Cu−1wt.% Ni alloys, in which the experimental values of $J_{corr}$ of both alloys showed a trend towards higher corrosion resistance for the most refined microstructure [29]. Al−4.5wt.%Cu [65] and Al−5wt.%Cu [61] also showed similar behavior, with higher corrosion resistance being associated with finer dendritic microstructures. This has been attributed to a more homogeneous distribution of $Al_2Cu$ in the Al rich phase (both in the eutectic mixture and in the Al rich dendritic matrix), that is, such intermetallics, when better distributed in refined dendritic arrangements, act as a protective barrier against corrosion. On the other hand, studies on the binary Al−5wt.%Ni alloy, showed an opposite behavior, that is, $J_{corr}$ of a coarse dendritic microstructure was lower than that of a refined dendritic microstructure. The authors concluded that the sample with the highest $J_{corr}$, i.e., that of the refined microstructure, showed higher pitting corrosion as compared to the sample with a coarse microstructure. These results are associated with the corresponding microstructural morphology and closely related to the Al-rich matrix, eutectic mixture fraction and quantity and distribution of the $Al_3Ni$ intermetallics that lead to the formation of local electrochemical galvanic cells with the Al-rich phase. According to the authors, the $Al_3Ni$ intermetallics has a double role in the corrosion action of an Al−Ni alloy, acting either as a corrosion barrier or as a galvanic cathode that accelerates the corrosion process. The role that dominates the corrosion process depends on the quantity and distribution of these intermetallic particles. When distributed in a fine and homogeneous way in the eutectic mixture, these particles can improve the pitting corrosion of an Al−Ni alloy [66].

The Al−6wt.%−Cu−5wt.% Ni alloy showed an average fraction of eutectic mixture of about 14.5%, using the ImageJ software as an area estimation tool. Binary alloys, Al−5wt.%Cu and Al−5wt.%Ni, presented eutectic fractions of about 12% and 80%, respectively. When evaluating the corrosion behavior of as-cast hypoeutectic alloys, knowing the electrochemical nature of the phases that compose the matrix and the eutectic is crucial for determining the cathodic-to-anodic area ($A_C/A_A$) ratio. As the $A_C/A_A$ ratio increases, $J_{corr}$ increases, thus reducing the corrosion resistance [67]. Based on the nobility and corrosion rate of the alloying elements involved (Cu and Ni) [68], the dendritic matrix should be less noble than the eutectic region. However, due to the supersaturated Cu and Ni content in solid solution in the matrix, the $\alpha$(Al) matrix also has a nobler nature. In this sense, three different microstructural regions can have distinct nobleness: (1) $\alpha$(Al) matrix rich in Cu and Ni; (2) Al-eutectic Cu-depleted; (3) Cu and Ni IMCs, where $\varphi_{corr}$ increases in the order of (2)→(1)→(3).

The presence of Cu in the $\alpha$(Al) matrix changed the $A_C/A_A$ configuration between the phases and constituents of the microstructure of the Al−6wt.%Cu−5wt.%Ni alloy. A supersaturated $\alpha$(Al) matrix with about 3 wt.% Cu (as shown in

**Table 2** Summary of experimental results such as cooling rate, microstructural aspects ($\lambda_1$, $\lambda_2$, $F_{IMC}$), corrosion potential ($\varphi_{corr}$), and corrosion current density ($J_{corr}$) of Al−6wt.%Cu−5wt.%Ni alloy

| Sample | Cooling rate/ (K·s$^{-1}$) | $\lambda_1$/μm | $\lambda_2$/μm | $F_{IMC}$/ % | $\varphi^*_{corr}$/ mV | $J^*_{corr}$/ (μA·cm$^{-2}$) | CR$^*$/ (cm$^2$·μA$^{-1}$) | $R_C$/ (μm·year$^{-1}$) |
|---|---|---|---|---|---|---|---|---|
| *P*5 | 14.71 | 22.53±3.4 | 10.43±1.8 | 14.23±0.6 | −550 | 0.88 | 1.14 | 9.94 |
| *P*20 | 1.3 | 83.35±15.08 | 19.15±3.2 | 13.58±0.7 | −560 | 1.20 | 0.83 | 13.6 |
| *P*50 | 0.26 | 124.23±19.12 | 26.55±3.5 | 11.75±0.8 | −532 | 1.82 | 0.54 | 20.6 |

*Measurement of potential vs Ag/AgCl at 25 °C

Fig. 11) seems to have strongly contributed to the beginning of pitting corrosion at the Al-eutectic phase, since it has anodic behavior as compared to that of the $\alpha$(Al) matrix and IMCs. Such information can be corroborated by the values of $\varphi_{corr}$ (vs SCE) reported in a study by BIRBILIS and BUCHHEIT [68], in which a solid solution Al−4wt.%Cu and pure Al were shown to have $\varphi_{corr}$ of −602 and −823 mV, respectively. Based on the corrosion rate per year ($R_C$) in Table 2, the best corrosion resistance is observed for a more refined microstructural arrangement (*P*5 sample), so it has been selected to explain how corrosion evolves. Figure 19 presents a scheme that exemplifies the microstructural morphology considering metallurgical and electrochemical aspects. The light gray region, located at the IMC/Al-eutectic interface, indicates where the pitting corrosion process has started. The SEM image in Fig. 19, shows that pitting corrosion starts at the Al-eutectic phase and then moves towards the Cu-depleted region. This behavior is like the intergranular corrosion mechanism, for which the corrosion is caused by a difference in the electrochemical potentials between the bulk of the grain and the grain boundaries, where intermetallic phases precipitate [69].

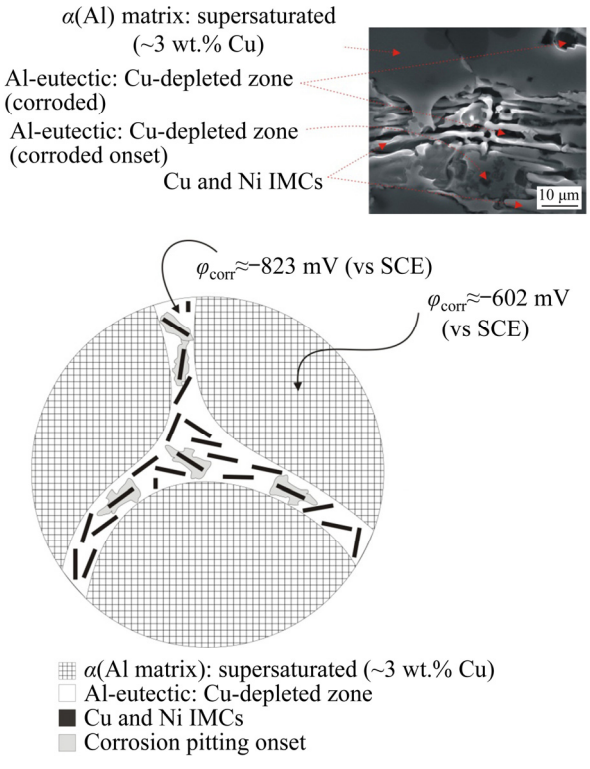


**Fig. 19** Schematic of path and onset of corrosion

In summary, the addition of Ni to the Al−5wt.%Cu alloy promoted a reduction in the average $J_{corr}$ value [29,70]. When evaluating the electrochemical behavior of the Al−6wt.%Cu−5wt.%Ni alloy, two different perspectives on the corrosion behavior can be drawn. Firstly, considering the morphology and the length scale of the matrix, the Al−6wt.%Cu−5wt.%Ni alloy is similar to the hypoeutectic Al−5wt.%Cu alloy [61], with lower corrosion current density associated with a more refined microstructural arrangement. Secondly, concerning the increase in nobility of the alloy with the addition of 5 wt.% Ni, $J_{corr}$ of the Al−6wt.%Cu−5wt.%Ni alloy is close to that of the Al−5wt.%Ni alloy [70]. In a recent work with the Al−15wt.%Cu−1wt.%Ni and Al−5wt.%Cu−1wt.%Ni alloys [29], it was also observed that the addition of Ni to Al−Cu alloys made them nobler, that is, $E_{corr}$ increased and $J_{corr}$ decreased, as compared to corresponding binary alloys [60,70].

Figure 20 shows SEM micrographs of Al−6wt.%Cu−5wt.%Ni alloy samples that were examined after the corrosion tests. It is worth mentioning that the microstructure of Al−6wt.%Cu−5wt.%Ni alloy is characterized by an essentially dendritic $\alpha$(Al) matrix and a eutectic mixture in the interdendritic regions, formed by Al-eutectic + IMCs (secondary phases): $Al_3Ni_2$, $Al_2Cu$ and $Al_7Cu_4Ni$. By analyzing Fig. 19, it can be seen that the corrosion process started in the interdendritic regions, and this visualization was possible due to the low severity of 0.06 mol/L NaCl solution used. The IMCs contain elements, such as Cu and Ni, that have a nobler potential as compared to that of the Al-eutectic phase. The IMCs have a cathodic character while the Al-eutectic phase has a more anodic one, resulting in galvanic corrosion. It is noted, therefore, that the corrosive process for this alloy starts in the eutectic region (interdendritic region), with the formation of a galvanic pair (Al-eutectic phase + IMCs), with localized corrosion prevailing. When the intermetallic phases are thinner and more evenly distributed, they result in a general protection against corrosion, which is the case of the *P*5 sample, which has a higher percentage of IMCs ((14.23±0.6)%), as shown in Table 2. In this sense, the fraction and distribution of IMCs in the eutectic phase seem to define the resulting corrosive behavior.

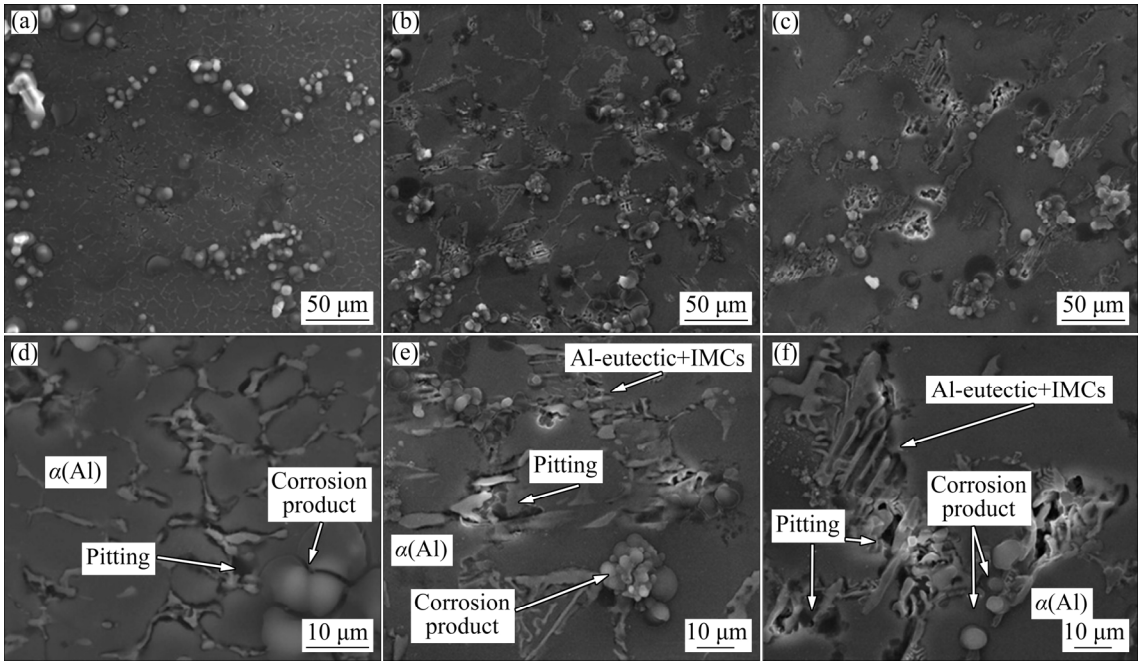


**Fig. 20** SEM micrographs of corroded samples *P*5 (a, d); *P*20 (b, e) and *P*50 (c, f) of Al−6wt.%Cu−5wt.%Ni alloy casting

## 4 Conclusions

(1) The macrostructure of DS Al−6.0wt.%Cu−5.0wt.%Ni alloy casting showed the columnar grains aligned along the heat flow direction, without any evidence of macrosegregation along the length of the casting. The microstructure was characterized by an $\alpha$(Al) dendritic matrix with interdendritic regions composed by a mixture of Al and $Al_3Ni_2$, $Al_2Cu$ and $Al_7Cu_4Ni$ IMCs. The high solidification cooling rates of the present experimental study inhibited the formation of $Al_3Ni$.

(2) Experimental growth laws have been derived relating the evolution of primary ($\lambda_1$) and secondary ($\lambda_2$) dendritic spacings along the length of the DS Al−6.0wt.%Cu−5.0wt.%Ni alloy casting to the solidification cooling rate ($\dot{T}$) and the growth rate ($V_L$): $\lambda_1 = 71.7\dot{T}^{-0.55}$; $\lambda_1 = 56V_L^{-1.1}$ and $\lambda_2 = 18\dot{T}^{-0.33}$; $\lambda_2 = 16.2V_L^{-0.66}$. The primary dendritic spacings were shown to be lower than those of Al−5.0wt.%Cu, Al−4.7wt.%Ni and Al−5.0wt.%Cu−1.0wt.%Ni alloys in the range of examined experimental cooling rates.

(3) The elongation to fracture ($\delta$) and the ultimate tensile strength ($\sigma_U$) along the length of the DS Al−6.0wt.%Cu−5.0wt.%Ni alloy casting were correlated with the inverse of the square root of $\lambda_1$ by Hall−Petch type experimental equations. Such properties were also compared with those of a binary Al−Cu alloy (Al−4.0wt.%Cu) in a similar range of $\lambda_1$, and the ternary alloy exhibited $\sigma_U$ values significantly higher as compared to those of the binary alloy. However, the tensile properties of the binary alloy were shown to be more sensitive to variations in $\lambda_1$ while the ternary alloy containing Ni has shown only slight increase in $\sigma_U$ for more decreased $\lambda_1$ values. It seems that the reinforcing effect caused by the addition of Ni surpasses that provided by the refinement of the dendritic microstructure.

(4) Corrosion tests carried out with samples of the Al−6.0wt.%Cu−5.0wt.%Ni alloy have shown that the corrosion process started in the interdendritic regions, with the IMCs indicating a nobler potential as compared to that of the Al-eutectic phase, with localized corrosion prevailing, i.e., galvanic corrosion. The higher fraction of IMCs as well as their fineness and better distribution have provided better protection against corrosion.

## Acknowledgments

The authors acknowledge CNPq - National Council for Scientific and Technological

Development (Grant: 407871/2018-7), CAPES - Coordenação de Aperfeiçoamento de Pessoal de Nível Superior, Brazil, for the financial support, as well as the Brazilian Nanotechnology National Laboratory - LNNano for the use of the X-ray diffractometer.

## References

[1] ENGIN S. Microstructure and mechanical properties of AlCuFe eutectic alloy [J]. Transactions of Nonferrous Metals Society of China, 2020, 30: 3183−3194.

[2] LIU T, LEAZER J D, BREWER L N. Particle deformation and microstructure evolution during cold spray of individual Al−Cu alloy powder particles [J]. Acta Materialia, 2019, 168: 13−23.

[3] CHEN S, WU Y, LI Y, CHEN M, ZHENG Q, ZHAN X. Study on 2219 Al−Cu alloy T-joint used dual laser beam bilateral synchronous welding: Parameters optimization based on the simulation of temperature field and residual stress [J]. Optics and Laser Technology, 2020, 132: 106481.

[4] ZHANG D K, ZHAO Y, DONG M Y, WANG G Q, WU A P, SHAN J G, MENG D Y, LIU X L, SONG J L, ZHANG Z P. Effects of weld penetration on tensile properties of 2219 aluminum alloy TIG-welded joints [J]. Transactions of Nonferrous Metals Society of China, 2019, 29: 1161−1168.

[5] ACOSTA G, VELEVA L, LÓPEZ J L, LÓPEZ-SAURI D A. Contrasting initial events of localized corrosion on surfaces of 2219-T42 and 6061-T6 aluminum alloys exposed in Caribbean seawater [J]. Transactions of Nonferrous Metals Society of China, 2019, 29: 34−42.

[6] FERREIRA I L, MOUTINHO D J, GOMES L G, ROCHA O L, GOULART P R, GARCIA A. Microstructural development in a ternary Al−Cu−Si alloy during transient solidification [J]. Materials Science Forum, 2010, 636−637: 643−650.

[7] OSÓRIO W R, MOUTINHO D J, PEIXOTO L C, FERREIRA I L, GARCIA A. Macrosegregation and microstructure dendritic array affecting electrochemical behavior of ternary Al−Cu−Si alloys [J]. Electrochimica Acta, 2011, 56: 8412−8421.

[8] LIU C T. Recent advances in ordered intermetallics [J]. Materials Chemistry and Physics, 1995, 42: 77−86.

[9] YANG H L, WATSON D, WANG Y, JI S X. Effect of nickel on the microstructure and mechanical property of die-cast Al−Mg−Si−Mn alloy [J]. Journal of Materials Science, 2014, 49: 8412−8422.

[10] STADLER F, ANTREKOWITSCH H, FRAGNER W, KAUFMANN H, PINATEL E R, UGGOWITZER P J. The effect of main alloying elements on the physical properties of Al−Si foundry alloys [J]. Materials Science and Engineering A, 2013, 560: 481−491.

[11] WEN J, CUI H Z, WEI N, SONG X J, ZHANG G S, WANG C M, SONG Q. Effect of phase composition and microstructure on the corrosion resistance of Ni−Al intermetallic compounds [J]. Journal of Alloys and Compounds, 2017, 695: 2424−2433.

[12] BOZORGI S, ANDERS K. Mechanical properties of high copper containing Al−Cu−Si cast alloys at elevated temperature [C]//Proc 16th International Aluminum Alloys Conference (ICAA16). Montreal, Canada: Canadian Institute of Mining, Metallurgy & Petroleum, 2018.

[13] ZHANG J Y, ZUO L J, FENG J, YE B, KONH X Y, JIANG H Y, DING W J. Effect of thermal exposure on microstructure and mechanical properties of Al−Si−Cu−Ni−Mg alloy produced by different casting technologies [J]. Transactions of Nonferrous Metals Society of China, 2020, 30: 1717−1730.

[14] LI Y G, YANG Y, WU Y Y, WANG L Y, LIU X F. Quantitative comparison of three Ni-containing phases to the elevated-temperature properties of Al−Si piston alloys [J]. Materials Science and Engineering A, 2010, 527: 7132−7137.

[15] KAYA H, GÜNDÜZ M, ÇADIRLI E, MARASLI N. Dependency of microindentation hardness on solidification processing parameters and cellular spacing in the directionally solidified Al based alloys [J]. Journal of Alloys and Compounds, 2009, 478: 281−286.

[16] OSÓRIO W R, FREIRE C M, GARCIA A. The effect of the dendritic microstructure on the corrosion resistance of Zn−Al alloys [J]. Journal of Alloys and Compounds, 2005, 397: 179−191.

[17] VIDA T A, FREITAS E S, BRITO C, CHEUNG N, ARENAS M A, CONDE A, DAMBORENEA J, GARCIA A. Thermal parameters and microstructural development in directionally solidified Zn-rich Zn−Mg alloys [J]. Metallurgical and Materials Transactions A, 2016, 47(6): 3052−3064.

[18] de SOUZA BAPTISTA L A, PARADELA K G, FERREIRA I L, GARCIA A, FERREIRA A F. Experimental study of the evolution of tertiary dendritic arms and microsegregation in directionally solidified Al−Si−Cu alloys castings [J]. Journal of Materials Research and Technology, 2019, 8(1): 1515−1521.

[19] KURZ W, FISHER D J. Dendrite growth at the limit of stability: Tip radius and spacing [J]. Acta Metallurgica, 1981, 29(1): 11−20.

[20] TRIVEDI R. Interdendritic spacing: Part II. A comparison of theory and experiment [J]. Metallurgical and Materials Transactions A, 1984, 15(6): 977−982.

[21] HUNT J D, LU S. Numerical modeling of cellular/dendritic array growth: Spacing and structure predictions [J]. Metallurgical and Materials Transactions A, 1996, 27(3): 611−623.

[22] D'ELIA F, RAVINDRAN C, SEDIAKO D, DONABERGER R. Solidification analysis of Al−5wt.%Cu alloy using in situ neutron diffraction [J]. Canadian Metallurgical Quarterly, 2015, 54(1): 9−15.

[23] WANG T, GAO T, ZHANG P, NIE J F, LIU X F. Influence of a new kind of Al−Ti−C master alloy on the microstructure and mechanical properties of Al−5Cu alloy [J]. Journal of Alloys and Compounds, 2014, 589: 19−24.

[24] GÜNDÜZ M, ÇADIRLI E. Directional solidification of aluminium−copper alloys [J]. Materials Science and Engineering A, 2002, 327: 167−185.

[25] RASHID A M, AMADEH A. Low temperature formation of

aluminide layers on nanocrystalline nickel [J]. Intermetallics, 2009, 17: 672−674.

[26] ILBAGI A, KHATIBI P D, SWAINSON I P, REINHART G, HENEIN H. Microstructural analysis of rapidly solidified aluminium−nickel alloys [J]. Canadian Metallurgical Quarterly, 2011, 50: 295−302.

[27] ALIMADADI H, KJARTANSDÓTTIR C, BURROWS A, KASAMA T, MOLLER P. Nickel−aluminum diffusion: A study of evolution of microstructure and phase [J]. Materials Characterization, 2017, 130: 105−112.

[28] GARCÍA-ESCORIAL A, LIEBLICH M. Microstructural characterization of $Ni_{75}Al_{25}$ and $Ni_{31.5}Al_{68.5}$ powder particles produced by gas atomization [J]. Journal of Alloys and Compounds, 2014, 586: s489−s493.

[29] RODRIGUES A V, LIMA T S, VIDA T A, BRITO C, GARCIA A, CHEUNG N. Microstructure and tensile/corrosion properties relationships of directionally solidified Al−Cu−Ni alloys [J]. Metals and Materials International, 2018, 24: 1058−1076.

[30] CANTÉ M V, CRUZ K S, SPINELLI J E, CHEUNG N, GARCIA A. Experimental analysis of the columnar-to-equiaxed transition in directionally solidified Al−Ni and Al−Sn alloys [J]. Materials Letters, 2007, 61: 2135−2138.

[31] FERREIRA I L, SIQUEIRA C A, SANTOS C A, GARCIA A. Theoretical and experimental analysis of inverse segregation during unidirectional solidification of an Al−6.2wt.%Cu alloy [J]. Scripta Materialia, 2003, 49: 339−344.

[32] FERREIRA I L, SANTOS C A, VOLLER V R, GARCIA A. Analytical, numerical, and experimental analysis of inverse macrosegregation during upward unidirectional solidification of Al−Cu alloys [J]. Metallurgical and Materials Transactions B, 2004, 35: 285−297.

[33] FERREIRA I L, GARCIA A, NESTLER B. On Macrosegregation in ternary Al−Cu−Si alloys: Numerical and experimental analysis [J]. Scripta Materialia, 2004, 50: 407−411.

[34] BOEIRA A P, FERREIRA I L, GARCIA A. Alloy Composition and metal/mold heat transfer efficiency affecting inverse segregation and porosity of as-cast Al−Cu alloys [J]. Materials and Design, 2009, 30: 2090−2098.

[35] MEHRABIAN R, FLEMINGS M C. Macrosegregation in ternary alloys [J]. Metallurgical Transactions, 1970, 1: 455−464.

[36] MOUTINHO D J, GOMES L G, ROCHA O L, FERREIRA I L, GARCIA A. Thermal parameters, microstructure and porosity during transient solidification of ternary Al−Cu−Si alloys [J]. Materials Science Forum, 2013, 730−732: 883−888.

[37] MURTY B S, KORI S A, CHAKRABORTY M. Grain refinement of aluminium and its alloys by heterogeneous nucleation and alloying [J]. International Materials Reviews, 2002, 49: 3−29.

[38] KARAKÖSE E, KESKIN M. Structural investigations of mechanical properties of Al based rapidly solidified alloys [J]. Materials and Design, 2011, 32: 4970−4979.

[39] WANG L, SUN Y, BO L, ZUO M, ZHAO D G. Effects of melt cooling rate on the microstructural and mechanical properties of Al−Cu alloy [J]. Materials Research Express, 2019, 6: 116507.

[40] ICHIKAWA R, OHASHI T, IKEDA T. Effects of cooling rate and supercooling degree on solidified structures of Al−Mn, Al−Cr and Al−Zr alloys in rapid solidification [J]. Materials Transactions−The Japan Institute of Metals−JIM, 1971, 12: 280−284.

[41] TOTTEN G E, MACKENZIE D S. Handbook of aluminum: Volume 1 – Physical metallurgy and processes [M]. New York: Marcel Dekker, 2003.

[42] REARDON A C. Metallurgy for the non-metallurgist [M]. 2nd ed. Ohio: ASM International, 2011.

[43] CHEN C L, THOMSON R C. The combined use of EBSD and EDX analyses for the identification of complex intermetallic phases in multicomponent Al−Si piston alloys [J]. Journal of Alloys and Compounds, 2010, 490: 293−300.

[44] WARMUZEK M. Chemical composition of the Ni-containing intermetallic phases in the multicomponent Al alloys [J]. Journal of Alloys and Compounds, 2014, 604: 245−252.

[45] KUNDIN J, EMMERICH H, WANG P, SCHMID-FETZER R. peculiarities of phase transitions and structure formation in a ternary Al−Cu−Ni alloy with four-phase peritectic reaction [J]. Journal of Metals, 2014, 66: 1502−1511.

[46] LLOYD G E. Atomic number and crystallographic contrast images with the SEM: A review of backscattered electron techniques [J]. Mineralogical Magazine, 1987, 51: 3−19.

[47] MOTLAGH E B, NASIRI H, KHAKI J V, SABZEVAR M H. Formation of metal matrix composite reinforced with nano sized $Al_2O_3$+Ni−Al intermetallics during coating of Al substrate via combustion synthesis [J]. Surface and Coatings Technology, 2011, 205: 5515−5520.

[48] ROCHA O L, SIQUEIRA C A, GARCIA A. Heat flow parameters affecting dendrite spacings during unsteady-state solidification of Sn−Pb and Al−Cu Alloys [J]. Metallurgical and Materials Transactions A, 2003, 34: 995−1006.

[49] CANTÉ M V, SPINELLI J E, FERREIRA I L, CHEUNG N, GARCIA A. Microstructural development in Al−Ni alloys directionally solidified under unsteady-state conditions [J]. Metallurgical and Materials Transactions A, 2008, 39: 1712−1726.

[50] KURZ W, FISHER D J. Fundamentals of solidification [M]. Zurich: Trans Tech Publications, 1998.

[51] BRITO C, COSTA T A, VIDA T A, BERTELLI F, CHEUNG N, SPINELLI J E, GARCIA A. Characterization of dendritic microstructure, intermetallic phases, and hardness of directionally solidified Al−Mg and Al−Mg−Si alloys [J]. Metallurgical and Materials Transactions A, 2015, 46: 3342−3355.

[52] FARIA J D, BRITO C C, COSTA T A P S, VERÍSSIMO N C, SANTOS W L R, DIAS FILHO J M S, GARCIA A, CHEUNG N. Influence in the microstructure and in the microhardness regarding the effects of adding 4%Ag in the Al−4%Cu unidirectionally solidified alloy [J]. Revista Matéria, 2015, 20: 992−1007. (in Portuguese)

[53] SILVA B L, GARCIA A, SPINELLI J E. Cooling thermal parameters and microstructure features of directionally solidified ternary Sn−Bi−(Cu,Ag) solder alloys [J]. Materials Characterization, 2016, 114: 30−42.

[54] EASTON M, STJOHN D. Grain refinement of aluminum alloys: Part I. The nucleant and solute paradigms—A review

of the literature [J]. Metallurgical and Materials Transactions A, 1999, 30: 1613−1623.
[55] CHANDRASHEKAR T, MURALIDHARA M K, KASHYAP K T, RAO P R. Effect of growth restricting factor on grain refinement of aluminum alloys [J]. The International Journal of Advanced Manufacturing Technology, 2009, 40: 234−241.
[56] ROHATGI S, TIWARI M, RATHI A, SHARMA A. Role of undercooling and effect of solute particles on grain refinement of aluminium alloys [J]. Indian Foundry Journal, 2015, 61: 31−37.
[57] KIM J T, SOPRUNYUK V, CHAWAKE N, ZHENG Y H, SPIECKERMANN F, HONG S H, KIM K B, ECKERT J. Outstanding strengthening behavior and dynamic mechanical properties of in-situ Al−$Al_3Ni$ composites by Cu addition [J]. Composites Part B, 2020, 189: 107891.
[58] CHEN C L, WEST G D, THOMSON R C. Characterization of intermetallic phases in multicomponent Al−Si casting alloys for engineering applications [J]. Materials Science Forum, 2006, 519−521: 359−364.
[59] KUNDIN J, WANG P, EMMERICH H, SCHMID-FETZER R. Investigation of Al−Cu−Ni alloy solidification: Thermodynamics, experiments and phase-field modeling [J]. The European Physical Journal Special Topics, 2014, 223: 567−590.
[60] BASAK C B, MEDURI A, BABU N H. Influence of Ni in high Fe containing recyclable Al−Si Cast alloys [J]. Materials Design, 2019, 182: 108017.
[61] OSÓRIO W R, SIQUEIRA C A, SANTOS C A, GARCIA A. The correlation between electrochemical corrosion resistance and mechanical strength of as-cast Al−Cu and Al−Si alloys [J]. International Journal of Electrochemical Science, 2011, 6: 6275−6289.
[62] BRITO C, VIDA T, FREITAS E, CHEUNG N, SPINELLI J E, GARCIA A. Cellular/dendritic arrays and intermetallic phases affecting corrosion and mechanical resistances of an Al−Mg−Si alloy [J]. Journal of Alloys and Compounds, 2016, 673: 220−230.
[63] YUE R, HUANG H, KE G Z, ZHANG H, PEI J, XUE G H, YUAN G Y. Microstructure, mechanical properties and in vitro degradation behavior of novel Zn−Cu−Fe alloys [J]. Materials Characterization, 2017, 134: 114−122.
[64] ASTM G102−89. Standard practice for calculation of corrosion rates and related information from electrochemical measurements [S]. ASTM Standard Test Methods (ASTM International), 2015.
[65] OSÓRIO W R, SPINELLI J E, FERREIRA I L, GARCIA A. The roles of macrosegregation and of dendritic array spacings on the electrochemical behavior of an Al−4.5wt.%Cu alloy [J]. Electrochimica Acta, 2007, 52: 3265−3237.
[66] OSÓRIO W R, PEIXOTO L C, CANTÉ M V, GARCIA A. Electrochemical corrosion characterization of Al−Ni alloys in a dilute sodium chloride solution [J]. Electrochimica Acta, 2010, 55: 4078−4085.
[67] STANSBURY E E, BUCHANAN R A. Fundamentals of electrochemical corrosion [M]. London: ASM International, 2000.
[68] BIRBILIS N, BUCHHEIT R G. Electrochemical characteristics of intermetallic phases in aluminum alloys an experimental survey and discussion [J]. Journal of The Electrochemical Society, 2005, 152: B140−B151.
[69] VARGEL C. Corrosion of aluminium [M]. Elsevier, 2004.
[70] OSÓRIO W R, PEIXOTO L C, CANTÉ M V, GARCIA A. Microstructure features affecting mechanical properties and corrosion behavior of a hypoeutectic Al−Ni alloy [J]. Materials and Design, 2010, 31: 4485−4489.

# 定向凝固 Al−6%Cu−5%Ni 合金的显微组织特征和力学、电化学行为

Adilson Vitor RODRIGUES[1,2], Thiago Soares LIMA[1], Talita Almeida VIDA[1], Crystopher BRITO[3], Amauri GARCIA[1], Noé CHEUNG[1]

1. Department of Manufacturing and Materials Engineering, University of Campinas - UNICAMP, Campinas, SP, 13083-860, Brazil;
2. Federal Institute of Education, Science and Technology of São Paulo - IFSP, Bragança Paulista, SP, 12903-600, Brazil;
3. São Paulo State University - UNESP, Campus of São João da Boa Vista, São João da Boa Vista, SP, 13876-750, Brazil

**摘　要**：在 Al−6%Cu 合金中添加 5.0% Ni(质量分数)，研究其对合金凝固时的冷却速率($\dot{T}$)和生长速率($V_L$)，显微组织中枝晶长度、金属间化合物(IMCs)的形貌和分布，以及最终性能的影响。研究在大冷却速率范围内制备的定向凝固 Al−6%Cu−5.0%Ni 合金铸锭沿长度方向的耐腐蚀性和拉伸性能。推导出一次枝晶间距($\lambda_1$)和二次枝晶间距($\lambda_2$)随 $\dot{T}$ 和 $V_L$ 的演变规律。采用 Hall−Petch 公式计算沿铸件长度方向的断后伸长率($\delta$)和极限抗拉强度($\sigma_U$)与 $\lambda_1^{-1/2}$ 的关系。在合金成分中添加 Ni 的强化效果优于细化枝晶组织的强化效果。在较高 $\dot{T}$ 下凝固的样品中形成细小的 IMCs，且均匀分布在枝晶间，这种典型的显微组织使样品具有最高的耐腐蚀性。

**关键词**：Al−Cu−Ni 合金；铸态显微组织；枝晶间距；拉伸强度；耐腐蚀性

**(Edited by Bing YANG)**